Speleothem record from Pentadactylos cave (Cyprus): new insights into climatic variations during MIS 6 and MIS 5 in the Eastern Mediterranean

C. Nehme, T. Kluge, S. Verheyden, F. Nader, I. Charalambidou, T. Weissbach, S. Gucel, H. Cheng, R.L. Edwards, L. Satterfield, et al.

Speleothem record from Pentadactylos cave (Cyprus): new insights into climatic variations during MIS 6 and MIS 5 in the Eastern Mediterranean

C. Nehme[1,10], Kluge. T.[2,#], Verheyden S.[3,10], Nader F.[4], Charalambidou I.[5], Weissbach T.[2], Gucel S.[6], Cheng H.[7,8], R.L. Edwards[8], Satterfield L.[9], Eiche E[#]., Claeys Ph[10].
1 - IDEES UMR 6266 CNRS, University of Rouen-Normandy, France. carole.nehme@univ-rouen.fr
2 - Institute of Environmental Physics, University of Heidelberg, Germany. tkluge@iup.uni-heidelberg.de; tweissbach@iup.uni-heidelberg.de
3 - Department of Earth and History of Life, Royal Institute of Natural Sciences (RBINS), Belgium. sophie.verheyden@naturalsciences.be
4 - Department of Earth Sciences, University of Utrecht, The Netherlands. f.h.nader@uu.nl
5 - Department of Life & Health Sciences, U. Nicosia, Cyprus. charalambidou.i@unic.ac.cy
6- Environmental Research Center, Near East University, Nicosia, Cyprus. sgucel@hotmail.com
7 - Institute of Global Environmental Change, U. Xi'an Jiaotong, China. cheng021@xjtu.edu.cn
8 - Department of Earth Sciences, University of Minnesota, USA. edwar001@umn.edu
9 - School of Environmental and Forest Sciences, University of Washington, Seattle, USA lauren.redwoodhill@gmail.com
10 - Analytical Environmental & Geo-Chemistry, Vrije Universiteit Brussel, Belgium. phclaeys@vub.be
now at Institute of Applied Geosciences, Karlsruhe Institute of Technology, Karlsruhe, Germany

Keywords: Middle-East, speleothems, Cyprus, stable isotopes, fluid inclusions, last Glacial/Interglacial, paleotemperatures, clumped isotopes

1- Introduction

The Eastern Mediterranean (EM) is located in a climatically sensitive region since small changes in regional atmospheric circulation may have significant and rapid changes in rainfall amount and effective infiltration (Bar-Matthews et al., 2003; Cheng et al., 2015). Whereas climatic changes in this region are reasonably known regarding spatial and temporal resolution for the Holocene (e.g. Frumkin et al., 1999, 2000; Verheyden et al., 2008a; Ayalon et al., 2002, 2013; Nehme et al., 2015; 2018; Cheng et al., 2015, Rowe et al., 2019, Keinan et al., 2019; Bar-Matthews et al, 2019), climatic information is more limited for the Last Glacial and Last Interglacial (Marine Isotope Stage- MIS 5e) and gets particularly poor prior to MIS 5e.

In this context, speleothems (e.g. stalagmites) are currently considered as the most suitable terrestrial archives for establishing high resolution proxy time-series in paleoclimate research (Genty et al., 2003; Cheng et al., 2012; Fairchild and Baker, 2012). Beyond qualitative trends, speleothems can also provide quantitative estimates of paleoclimate data (temperature and rainfall amount) either through cave-specific proxy calibration (Tremaine et al., 2011) or through the isotopic analysis of fluid inclusions trapped within the carbonate speleothems at the time of their formation (Matthews et al., 2000; Verheyden et al., 2008b; Vonhof et al., 2006; Dublyansky and Spötl, 2009). Moreover, the application of clumped isotopes on associated calcite provides an additional control on the cave temperatures and its variation at the time of speleothem formation (Affek et al., 2008; Meckler et al., 2015; Kluge et al., 2020).

This contribution presents a new stalagmite stable isotope data ($\delta^{13}C$ and $\delta^{18}O$) from Pentadactylos cave (Cyprus), which provides a high-resolution and well-dated record for the Northern Levant region covering the time period from 175 to 163 ka, 141 to 132 ka and 127 to 110 ka. The combined measurements of calcite $\delta^{13}C$ and $\delta^{18}O$ and fluid inclusions isotope values (δD; $\delta^{18}O_w$), together with carbonate clumped isotopes (Δ_{47}), allow the estimation of the amplitude of the temperature rise between the end of the Penultimate Glacial and the Last Interglacial optimum. This record also allows to quantitatively understand the variations of the calcite $\delta^{18}Oc$ values through time. The different controls on the oxygen isotopic composition of the calcite ($\delta^{18}Oc$) during MIS 6 and MIS 5 (Mediterranean sapropels, rainfall amount, atmospheric circulation) will also be discussed in the Eastern Mediterranean (EM) context.

2- State of the art

2.1. The last Glacial (G)-Interglacial (IG) in the Mediterranean region

The last G-IG cycle covers Marine Isotope Stages (MIS) 6 (185-135 ka; Ehlers and Gibbard, 2007) and 5 (130-75 ka). During Marine Isotope Substage 6e (ca.179–165 ka; Margari et al., 2010), sea-level was –40 to –60 m relative to present (Thompson and Goldstein, 2006). The Mediterranean basin experienced

overall wetter conditions than previously thought (Chedadi and Rossignol-Strick, 1995), concurrent with glacial conditions in northern latitude regions (Ehlers et al., 2011). The overall wet conditions are the result of enhanced ITCZ activity through an intensified monsoon activity at the Nile Headwaters and concurrent with enhanced rainfall over the entire basin (Kallel et al., 2000). Although sapropel layers, an organic-rich sediment, in the EM basin are generally deposited during cycles of extreme wet periods (Emeis et al., 2003; Ziegler et al., 2010), the atypical sapropel S6 during the glacial MIS6 is a result of freshwater input, mostly from the Nile discharge, inducing lower $\delta^{18}O$ values in the seawater and consequently in EM rainwater and speleothems.

Marine cores revealed the existence of D-O-like climatic oscillations related to shifts in atmospheric circulation during the early and mid-MIS 6 (~178–150 ka; Margari et al., 2010; Stocker and Johnsen, 2003; Barker et al., 2011). These oscillations, sensitively mark some of the terrestrial records in the Central and EM basins reflecting millennial and sub-millennial rainfall and/or temperature variability (Tzedakis et al., 2009; Roucoux et al., 2011; Regattieri et al., 2014; Nehme et al., 2018). The late-MIS 6 (ca. 150-135 ka) was generally colder with a reduction of millennial variability as the climate reached more stable maximum glacial conditions (Bar-Matthews et al., 2003; Regattieri et al., 2014). This relative stability ended with the deglaciation (Termination - TII, ca. 135-130 ka), which is well-recorded in south-Levant speleothems (Bar-Matthews et al., 2003). Mediterranean marine cores suggest a temperature change of roughly 12°C between MIS 6 and MIS 5 (Emeis et al., 2003). Villars cave speleothems in North-Western Europe indicate a similar temperature difference for this deglaciation of about 13.2 to 14.6 ± 2.6°C (1σ) (Wainer et al., 2011). To date, no terrestrial temperature estimate is available for the penultimate G/IG cycle (MIS 6 to MIS 5e) in the Levant region.

The succeeding interglacial (MIS-5e) period (129-116 ka; Dutton and Lambeck, 2012; Masson-Delmotte et al., 2013) is generally characterized by a minimal ice volume, with a sea-level of 4-6 m higher than present (Kopp et al., 2009, Waelbroeck et al. 2002) and a global mean surface temperature of 1-2°C above the Holocene reference (Otto-Bliesner et al., 2013). The Mediterranean basin experienced warm conditions during the MIS 5e period with the deposition of the sapropel S5 (Rohling et al., 2002, 2015; Scrivner et al., 2004) and enhanced rainfall (Kallel et al., 2000). The linkage between sapropel deposition (marine environment) and the Levant terrestrial records is expressed in the similar timing of the deposits with an increase in speleothem deposition (growth rate) (Ayalon et al., 2002; Bar-Matthews et al., 2003; Nehme et al., 2015) occurring simultaneously with low $\delta^{18}O$ values registered in speleothems, demonstrating that both land and sea systems simultaneously experienced enhanced rainfall and fresh water input during this period (Bar-Matthews et al., 2019).

In the EM, the LIG (Eemian) started around 128 ka within age uncertainties (Bar-Matthews et al., 2003; Tzedakis et al., 2004, 2009). The related wet phase is supported by a general increase in speleothem growth rates, also observed in the Central (Drysdale, et al. 2009; Regattieri et al., 2014; Columbu et al., 2017) and Western Mediterranean (Dimitriu et al., 2018; Columbu et al., 2019). Except for the Dim speleothem, Southern Turkey (Rowe et al., 2020), which partially grew during the deglaciation and the LIG onset until 128 ka, no highly resolved terrestrial record covers the LIG period and its demise in the Northern Levant. The wet/warm conditions along the Levant seems to be relatively stable in general as shown in Peqiin and Soreq speleothem records (128-126 ka; Bar-Matthews et al., 2003, 2019) as well as in Kanaan cave, Lebanon (Nehme et al., 2015). To check for possible regional discrepancies, related to differences in location, atmospheric circulation patterns, local effect (orography, rainfall gradient) or differential influence of sapropel events on terrestrial records regarding the LIG onset, length and demise as well as the climatic variations during the last glacial MIS 6, it is crucial to investigate new records. The new paleoclimatic data will expand the spatial resolution of the available paleoclimatic information in the EM, in particular in the Northern Levant basin.

2.2. Speleothem proxies in general and in the Mediterranean

Useful proxies in the speleothems archive for paleoclimate reconstruction includes elemental ratios, $\delta^{13}C$ and $\delta^{18}O$ values, growth rate assessments, fluid inclusions isotopes, clumped isotopes, and others (Fairchild and Baker, 2012). Speleothem growth can be a proxy by itself and has three significant determinants: i) calcite saturation (Ca^{2+} and HCO_3-concentrations) depending on CO_2 degassing, ii) temperature and iii) water supply rate (Baker et al., 1998; Dreybrodt, 1988; Genty et al., 2001). Rainfall amount and temperature have an important influence on soil biological activity and consequently on CO_2 production driving the dissolution and precipitation processes. Therefore, warm and humid conditions are generally seen as ideal for speleothem deposition (Dreybrodt, 1988; Baker and Smart, 1995; Genty et al., 2006). Warm and humid conditions will increase the growth rate of speleothems. Speleothem diameter can also be used to infer climatic conditions because it is related to the dripwater supply, and thus to the effective infiltration, and to the saturation state (Dreybrodt, 1988, 1999). Large stalagmite diameters are related to wetter periods or periods with higher calcite saturation of the water. A minimal diameter relates to drier periods or periods with minimal calcite saturation.

Carbonate $\delta^{18}O$ values are amongst the most often used speleothems proxies. Unraveling the factors controlling the $\delta^{18}O$ signal in speleothems, however, can be complex (McDermott, 2004; Fairchild et al., 2006; Lachniet, 2009). In the Levant, more negative speleothem $\delta^{18}O$ values are associated with wetter conditions, while less negative speleothem $\delta^{18}O$ is generally ascribed to drier periods with lower rainfall amounts (Ayalon et al., 2002; Verheyden et al., 2008a; Cheng et al., 2015; Nehme et al. 2015, 2018; Bar-Matthews et al., 2019). Important variations in $\delta^{18}O$ values have also been linked to changes in the source of the water vapour and/or changes in storm trajectories (Frumkin et al., 1999; McGarry et al., 2004; Kolodny et al., 2005).

Generally, variations in $\delta^{13}C$ values can be the result of several factors: soil biogenic CO_2, a mix between C3/C4 vegetation, reduced or increased soil vegetation, increased residence time and carbonate dissolution, change in soil respiration rate, and/or seasonality. In the EM, $\delta^{13}C_{calcite}$ variations are mainly linked to changes in soil biogenic CO_2 through changes in local effective hydrologic conditions (Frumkin et al., 2000; Bar-Matthews et al., 2003; Verheyden et al., 2008a; Cheng et al., 2015).

Quantitative estimates of temperature and/or vegetation changes are generally difficult due to the existence of non-equilibrium deposition processes in at least some speleothems influencing the isotopic composition (Mickler et al., 2006; Affek et al., 2014). However, under continuous humid conditions speleothems are more likely to be deposited close to equilibrium, whereas and during drier periods, non-equilibrium formation may be significant (Verheyden et al., 2008c, Lachniet et al., 2009).
Another possibility for reconstruction of paleotemperature changes from speleothems is given by clumped isotope analysis (Affek et al., 2008; Affek, 2012; Meckler et al., 2014). Carbonate clumped isotopes refer to heavy isotopologues that include two or more rare isotopes. They are quantified with the Δ value ($=R/R_{stochastic}$) that describes their overabundance relative to the stochastic distribution (Eiler, 2011). Speleothem studies using clumped isotopes can be subdivided in two groups: i) direct application as absolute or relative temperature proxy in case of equilibrium mineral formation (Daeron et al., 2019) or if disequilibrium stays constant (Affek et al., 2008), and ii) for detection and correction of variable disequilibrium (Wainer et al., 2011; Kluge and Affek, 2012; Affek et al., 2014).
Fluid inclusions in speleothems as remnants of ancient dripwater record the water isotopic composition from which they form. Since dripwater is closely related to the surface rainwater (Genty et al., 2014; Affolter et al., 2015), isotopic composition may be used to recover ancient rainwater isotopic composition if calcite contains sufficient water, i.e. >0.3 µl/analysis. McGarry et al. (2004) studied fluid inclusion isotope values in three caves in Israel/Palestine during the last 140 ka and found correspondences to the global meteoric water line and the Mediterranean meteoric water line in varying climate stages.

3- Current climatic settings of the Eastern Mediterranean

The EM climate is currently influenced by the Atlantic westerlies, which bring in moist winds associated with extra-tropical cyclones. These originate in the Atlantic and track east across the Mediterranean Sea, forming a series of sub-synoptic low-pressure systems (Alpert et al., 2005). In winter, outbreaks of cold air plunging south over the relatively warm Mediterranean Sea enhance cyclogenesis and create the Cyprus Low. These low-pressure systems drive moist air onshore, generating intense orographic rainfall across the Levant coast. The duration, intensity, and tracks of these storm systems strongly influence the amount of rainfall in this region. On the island of Cyprus, the climate is warm temperate in the western part and arid in its eastern side according to the Köppen–Geiger Climate Classification (Kottek et al., 2006). Mean monthly temperatures range from 21°C along the coast to 15°C at the Kyrenia Range. The climate is seasonal, with relatively wet winters (November to March) and dry, hot summers. The annual precipitation reaches 600 mm along the Kyrenia Mountains at 1000 m above sea-level (asl) and up to 1000 mm on the Troodos (1952 m asl) summit (Cailhol et al., 2019). Both mountain ranges (Fig. 1B and C) receive orographic-driven rainfall mostly from northern and northwestern winds. Despite its northern situation in the EM, local climate is drier than the North-Levant coast where annual rainfall varies from 700 to 1400 mm on Mount-Lebanon (Nehme et al., 2019).

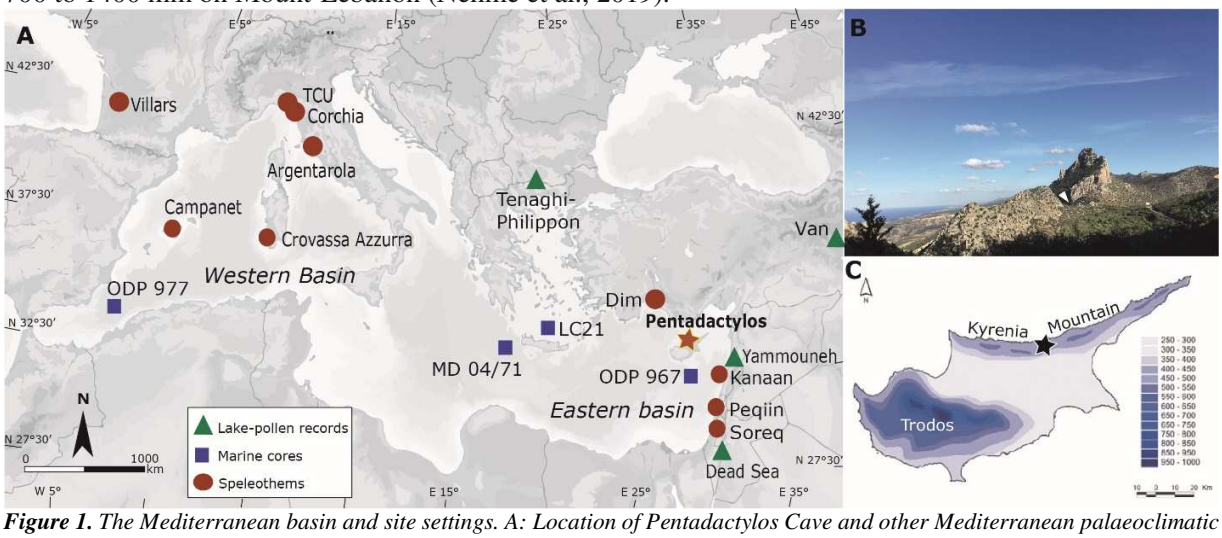

Figure 1. *The Mediterranean basin and site settings. A: Location of Pentadactylos Cave and other Mediterranean palaeoclimatic records spanning Marine Oxygen Isotope Stage (MIS) 6 and MIS 5. Speleothems: Villars (Wainer et al., 2011), Crovassa Azzurra (Columbu et al., 2019), Campanet (Dimitru et al., 2018), Tana Che Urla (TCU) (Regattieri et al., 2014), Argenterola (Bard et al., 2002), Dim (Rowe et al., 2020), Peqiin (Bar-Matthews et al., 2003), Soreq (Ayalon et al., 2002), Kanaan (Nehme et al., 2015, 2018),. Lacustrine records: Dead-Sea/Lake Lisan (Kiro et al., 2017), the Yammouneh paleolake (Gasse et al., 2015), Lake Van (Litt et al., 2014), and the Ioaninna (Roucoux et al., 2011) and Tenaghi-Philippon (Tzedakis et al., 2003, 2009) paleo lakes. Marine cores: M40-71 (Emeis et al., 2003), ODP 968 (Ziegler et al., 2010), ODP 967 (Chedadi and Rossignol-Strick, 1995; Emeis et al., 2003; Scrivner et al., 2004), ODP 977/A (Martrat et al., 2004, 2014). B: photo of the Pentadactylos peaks and the white arrow showing the entrance to the Cave. C: map of the annual weighted mean precipitation of Cyprus (Interwies and Görlitz, 2012).*

4- Cave site and sample description

The Pentadactylos Cave (35°17'22.13"N, 33°28'18.49"E) is located at 800 m asl in the central part of the Kyrenia Range (1023 m altitude, at the Northern coast of Cyprus (Fig. 1B). This mountain range with a West-East direction faces the northern Levant sea-basin and include newly discovered caves developed within Triassic to Cretaceous dolomitic limestone (Cailhol et al., 2019). The cave of 200 m depth comprises few detrital deposits, non-active speleothems (draperies) and stalagmites on fallen blocks. The two adjacent Penta stalagmite samples were retrieved from a 2 m-height chamber at 50 m depth from the entrance and with. ca 200 m of limestone overburden. Relative humidity was not measured in Pentadactylos cave, but was found to be between 88.6% closest to the entrance and up to 99.9% in the deepest cave parts of Smoky Cave, another cave in the Kyrenia range at similar altitude and with similar morphology (Cailhol et al., 2019. The Kyrenia Range is covered with a typical Mediterranean sparse 'garrigue' forest (i.e. pine shrubs) with sufficient soil thickness to ensure soil biological activity.

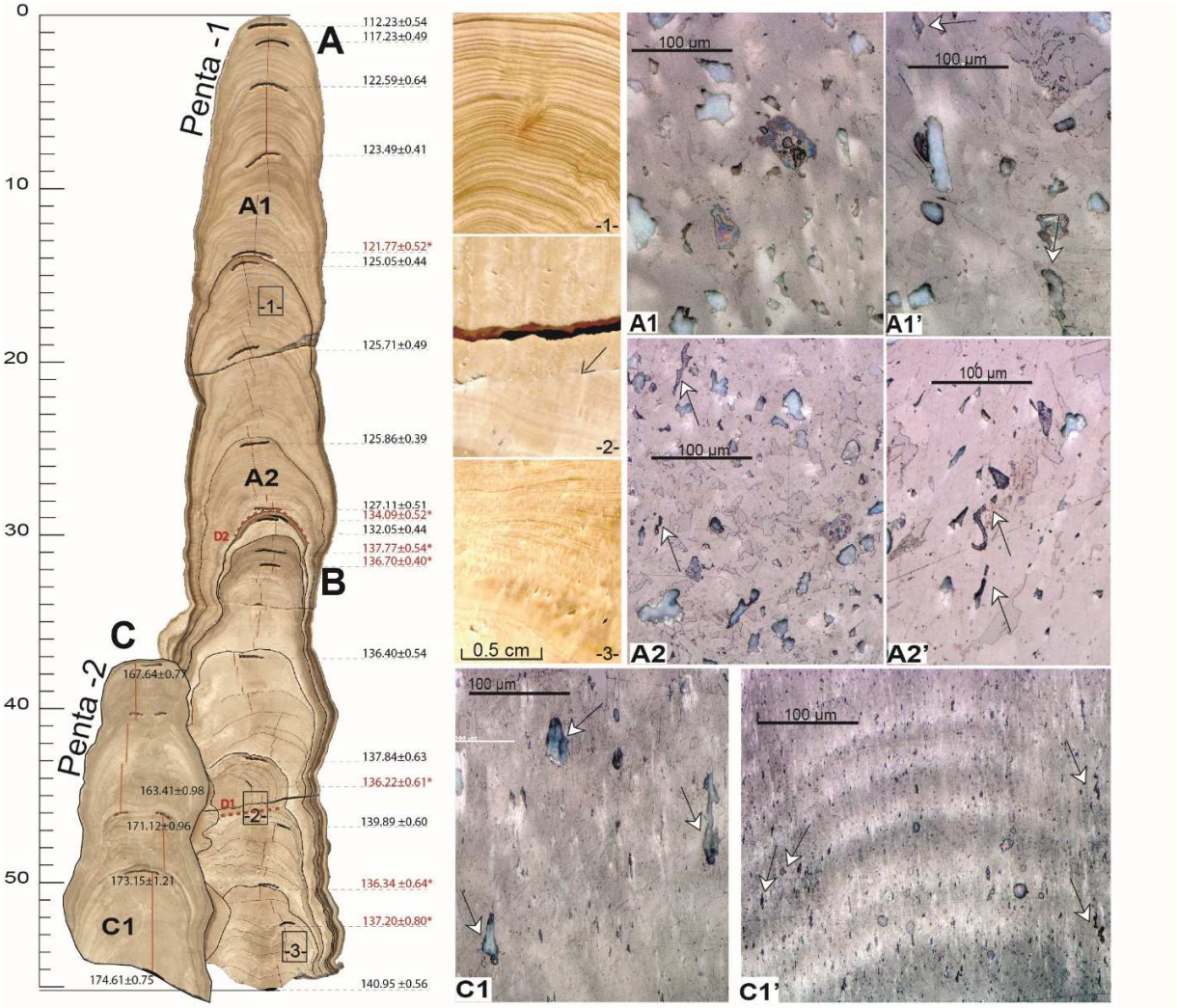

Figure 2. *Petrographic sections of the speleothem Penta-1 and Penta-2 showing from left to right: an image scan of the speleothem, the stable isotopes sampling track (red line), the location of the U–Th datings, location of photos 1, 2 and 3 showing the structure of the calcite laminae at 15 cm (photo 1), 46 cm (photo 2) and 53 cm (photo 3) depths. Locations of A1, A2 and C1 microscope images along the speleothem growth axis, are thin section photos with an indication of the identified large fluid inclusions (arrows). Discontinuities D1 and D2 as well as ages considered outliers are marked in red.*

Stalagmites Penta-1 and Penta-2 were cut along their growth axis and petrographically studied. The Penta-1 sample is 56.1 cm long and comprises two petrographic segments A and B (Fig. 2). Segment A, i.e. the upper part of Penta-1, is 30 cm long with a regular diameter of 6 to 7 cm wide. The segment comprises a laminated structure of alternating white and brown laminae with a porous texture, a dominance of columnar fabric and no post-crystallization disturbances. Segment B, i.e. the basal part of stalagmite Penta-1, is 26.5 cm long and has a diameter of ~7 cm at the basal part to ~4 cm at the top. It displays a laminated structure with alternating white and brown laminae at its top part and some post-crystallization disturbances characterized by microcrystalline calcite and dissolution horizons, especially in the basal part (Fig. 2-photo 3). Between 43 and 46 cm depth, perturbations in the sedimentary structure are due to the interlinked growth of both stalagmites, i.e. part of the side of the Penta 2 stalagmite is imprinted in the Penta 1 stalagmite and leads to circular structures (Fig.2 - photo 2) in the longitudinal section. Penta-2 (segment C) is 28 cm long, has a regular diameter of 4-5 cm and consists of a laminated structure of alternating white and brown laminae with a porous texture. Columnar fabrics are dominating with no post-crystallization disturbances. Thin sections of 80 to 100 µm thickness of the base of segments

A and C show a high concentration of fluid inclusions (Fig. 2-photos A1; A2). In segment A, these inclusions are up to 40 µm long and are situated between columnar calcite crystals. In Segment C, fluid inclusions of more than 50 µm length are clearly identified with a higher concentration of inclusions along the stalagmite flanks (Fig.2-photo C1).

Two discontinuities are observed along the growth axis of Penta-1. The discontinuity D1 at 46 cm depth is a break in the stalagmite (Fig.2, Photo 2). There, a side part of the Penta-2 stalagmite is imprinted in the Penta-1 stalagmite with re-dissolved calcite and no clear laminated structure (Fig. 2-photo 2). Another discontinuity D2 is clear at 28 cm depth with a brownish dark lamina and contrasting the lamination in part A2 of Penta-1 (Fig. 2). Discontinuity D2 is marked by a higher detrital content (Table 1).

5-Methods

5.1. U-series dating

25 ages were determined at Xi'an Jiaotong University (China), using the procedures for uranium and thorium chemical separation and purification described in Edwards et al. (1987) and Cheng et al. (2013; 2016). 100-150 mg powdered calcite samples were collected with a dental drill from 24 levels along or close to the growth axis of the speleothem, except for one sample drilled off the growth axis (Pentad-17).

Table 1. *Uranium-Thorium dating results. The uncertainty is given as 2σ error. U decay constants: l^{238} = 1.55125x10-10 (Jaffey et al., 1971) and l^{234}=2.82206x10-6 (Cheng et al., 2013). Th decay constant: l230=9.1705x10-6 (Cheng et al., 2013).*$\delta^{234}U=([^{234}U/^{238}U]$ activity–1)x1000.**δ^{234}Uinitial was calculated based on ^{230}Th age (T), i.e.,$\delta^{234}Uinitial=\delta^{234}Umeasured$ x $el^{234}xT$. Corrected ^{230}Th ages assume the initial $^{230}Th/^{232}Th$ atomic ratio of 4.4 ±2.2 x10-6 corresponding to a material at secular equilibrium with the bulk earth $^{232}Th/^{238}U$ value of 3.8. The $^{230}Th/^{232}Th$ error is arbitrarily assumed to be 50%. ***B.P. stands for "Before Present" where the "Present" is defined as the year 1950 A.D. Samples with (*) were considered as outliers.*

Sample Number	Depth mm	^{238}U (ppb)	^{232}Th (ppt)	^{230}Th / ^{232}Th (atomic x10^{-6})	$\delta^{234}U$* (measured)	^{230}Th / ^{238}U (activity)	^{230}Th Age (yr) (uncorrected)	^{230}Th Age (yr) (corrected)	$\delta^{234}U_{initial}$** (corrected)	^{230}Th Age (yr BP)*** (corrected)
Pentad-14	4	134.1 ±0.1	1359 ±27	1231 ±25	153.3 ±1.2	0.7568 ±0.0018	112539 ±513	112294 ±540	210 ±2	112226 ±540
Penta-24a	14	179.0 ±0.2	1970 ±39	1125 ±23	120.1 ±1.3	0.7511 ±0.0013	117575 ±448	117301 ±487	167 ±2	117232 ±487
Pentad-13	38	162.7 ±0.2	2802 ±56	765 ±15	156.6 ±1.3	0.7991 ±0.0018	123067 ±576	122656 ±643	221 ±2	122588 ±643
Pentad-12	78	161.6 ±0.1	614 ±12	3501 ±71	164.8 ±1.1	0.8063 ±0.0012	123250 ±410	123160 ±414	233 ±2	123092 ±414
*Pentad-11**	*135*	*158.4 ±0.2*	*798 ±16*	*2651 ±53*	*175.0 ±1.2*	*0.8095 ±0.0017*	*121964 ±520*	*121846 ±526*	*247 ±2*	*121778 ±526*
Pentad-10	141	167.5 ±0.1	692 ±14	3277 ±66	175.2 ±1.2	0.8216 ±0.0013	125211 ±432	125114 ±437	249 ±2	125046 ±437
Pentad-09	189	165.5 ±0.1	696 ±14	3187 ±65	161.0 ±1.2	0.8127 ±0.0014	125879 ±482	125779 ±487	230 ±2	125711 ±487
Pentad-08	243	176.6 ±0.2	782 ±16	3083 ±63	180.4 ±1.2	0.8287 ±0.0022	126034 ±663	125931 ±667	257 ±2	125863 ±667
Pentad-07	283	136.9 ±0.1	1000 ±20	1795 ±36	133.0 ±1.1	0.7955 ±0.0014	127353 ±500	127174 ±515	190 ±2	127106 ±515
*Pentad-19**	*287*	*290.0 ±0.3*	*337 ±7*	*12758 ±267*	*229.7 ±1.3*	*0.8982 ±0.0015*	*134185 ±522*	*134159 ±522*	*335 ±2*	*134091 ±522*
Pentad-06	289	286.7 ±0.2	257 ±5	16743 ±356	251.9 ±1.3	0.9097 ±0.0012	132338 ±437	132319 ±437	366 ±2	132251 ±437
*Pentad-18**	*307*	*347.9 ±0.4*	*693 ±14*	*7759 ±158*	*260.6 ±1.4*	*0.9372 ±0.0017*	*137880 ±582*	*137838 ±582*	*385 ±2*	*137770 ±582*
*Pentad-05**	*315*	*304.6 ±0.2*	*391 ±8*	*11853 ±240*	*247.0 ±1.2*	*0.9218 ±0.0010*	*136798 ±404*	*136770 ±405*	*363 ±2*	*136702 ±405*
Pentad-04	368	139.1 ±0.1	459 ±9	4351 ±89	186.0 ±1.2	0.8699 ±0.0015	136548 ±535	136473 ±538	273 ±2	136405 ±538
Pentad-03	428	184.4 ±0.1	881 ±18	2954 ±60	163.2 ±1.2	0.8556 ±0.0018	138024 ±627	137912 ±631	241 ±2	137844 ±631
*Pentad-17**		*119.6 ±0.1*	*239 ±5*	*7005 ±150*	*163.8 ±1.3*	*0.8506 ±0.0017*	*136336 ±616*	*136289 ±616*	*241 ±2*	*136221 ±616*
Pentad-16	474	161.1 ±0.1	147 ±3	15670 ±354	170.2 ±1.3	0.8677 ±0.0016	139989 ±602	139967 ±602	253 ±2	139899 ±602
*Pentad-02**	*509*	*114.8 ±0.1*	*2462 ±49*	*659 ±13*	*165.9 ±1.2*	*0.8570 ±0.0021*	*137784 ±724*	*137281 ±804*	*244 ±2*	*137213 ±804*
*Pentad-15**	*522*	*133.0 ±0.1*	*745 ±15*	*2554 ±52*	*183.7 ±1.3*	*0.8679 ±0.0018*	*136541 ±639*	*136412 ±644*	*270 ±2*	*136344 ±644*
Pentad-01	557	144.8 ±0.1	125 ±3	17239 ±431	210.9 ±1.3	0.9059 ±0.0015	141037 ±564	141017 ±564	314 ±2	140949 ±564
Pentad-23	546	195.6 ±0.2	289 ±6	10551 ±216	182.3 ±1.2	0.9468 ±0.0017	163519 ±768	163485 ±768	289 ±2	163416 ±768
Pentad-22	571	190.8 ±0.2	248 ±5	11620 ±240	137.9 ±1.2	0.9158 ±0.0021	167748 ±981	167716 ±980	221 ±2	167647 ±980
Pentad-21	625	239.5 ±0.2	441 ±9	8036 ±163	109.5 ±1.2	0.8968 ±0.0018	171239 ±961	171194 ±961	177 ±2	171125 ±961
Pentad-20	656	150.2 ±0.2	963 ±19	2474 ±50	172.5 ±1.6	0.9624 ±0.0024	173368 ±1209	173222 ±1212	281 ±3	173153 ±1212
Pentad-00	711	109.0 ±0.1	167 ±4	10485 ±224	181.6 ±1.2	0.9744 ±0.0014	174720 ±751	174685 ±751	297 ±2	174617 ±751

The data were obtained on a Thermo Neptune Plus multicollector inductively coupled plasma mass spectrometers (MC-ICP-MS) following procedures modified from Cheng et al. (2013). Ages are calculated from time of analysis (2018) with an uncertainty at the 2σ level, typically between 400 and 1000 a (Table 1). The stratigraphic uncertainties are less than 1.5 mm. The age model was constructed using the Constructing Proxy Records from Age models (COPRA) routine (Breitenbach et al., 2012), based on polynomial interpolation and 5000 Monte Carlo simulations for each segment of the stalagmite (Fig. 3). The polynomial function generates a monotonously positive depth-age slope (Breitenbach et al., 2012) with the assumption that all dates should be in chronological order (within errors). The median and

2.5% and 97.5% confidence intervals are based on 5000 Monte Carlo simulations. COPRA handles multiple hiatuses, as long as each is bracketed by at least two dates, which is the case for this sample.

5.2. Calcite and water stable isotopes measurements

739 speleothem calcite samples with 125 duplicates (92% replicability) were sampled along the growth axis (Fig. 2) for $\delta^{13}C$ and $\delta^{18}O$ measurements and were drilled along the speleothem central axis with a 0.5-1 mm resolution using a Merchantek Micromill mounted on a Leica microscope. Between every sample, the drill bit and sampling surface were cleaned with compressed air. The samples were analyzed together with modern calcite samples using either a Nu Carb carbonate device coupled to a Nu Perspective MS at the Vrije Universiteit Brussel or a Thermo Gas Bench II connected to a Thermo Delta Advantage mass spectrometer in continuous flow mode at Karlsruhe Institute of Technology (Germany). Analytical uncertainties were better than 0.1‰ (1σ) for oxygen and 0.05‰ (1σ) for carbon on both instruments. All $\delta^{18}O$ and $\delta^{13}C$ values are calibrated against Vienna Pee-Dee Belemnite (V-PDB) and are reported in permil (‰) relative to VPDB. The stalagmite was tested for isotopic equilibrium conditions by carrying out Hendy tests (Hendy, 1971) at twelve different heights along the speleothem axis (Appendix S3).

The Pentadactylos Cave showed insufficient active water seepage to sample during the fieldwork. Therefore, nine seepage and water samples from nearby caves and springs were collected in December 2018 for $\delta^{18}O$ and δD measurements in hermetically sealed glass bottles. Isotope measurements were performed at the Vrije Universiteit Brussel on a Picarro L2130-i analyzer using the cavity ring–down spectroscopy (CRDS) technique (Van Geldern and Barth Johannes, 2012). All values are reported in permil (‰) relative to Vienna standard mean ocean water (VSMOW). Analytical uncertainties (1σ) were better than 1‰ for δD and 0.1‰ for $\delta^{18}O$.

5.3. Fluid inclusions stable isotope (H-O) analyses

21 calcite samples, from 9 levels in Penta-1 and Penta-2 were measured using a custom-built extraction line connected to a (Picarro L2130i) analyzer using cavity ring down spectroscopy (WS-CRDS). This technique allows to simultaneously measure hydrogen and oxygen isotopes for minute water amounts released from calcite. The extraction line follows the design of Affolter et al. (2014) and is described in detail in Weißbach, 2020). In brief, the calcite samples were hydraulically crushed and the released fluid inclusion water instantly vaporized in the heated extraction system and transferred to the analyzer. Reference water injections with known $\delta^{18}O$ and δD values were used for calibration and quality control. µl-sized glass capillaries were used for high-precision water amount calibration (on the order of 10^{-8}l) and isotopic control. The overall precision of fluid inclusion water analyses is 0.5‰ for $\delta^{18}O$ and 1.5‰ for $\delta^{2}H$ if fluid water amounts are 0.5-1µl and 0.25‰ for $\delta^{18}O$ and 1‰ for $\delta^{2}H$ for fluid water amounts >1µl (Weißbach, 2020).

5.4. Clumped Isotopes

Clumped isotope measurements were performed on aliquots of the powder (>100 mg each) produced during the fluid inclusion analysis of samples 7b, 6b, 4b and 3 (Table 2). The sample treatment follows Weise and Kluge (2020). Calcite samples of ca. 3 mg were individually reacted with 105% phosphoric acid (~1 ml / sample) in a stirred glass reaction vessel for 10 min at 90°C. The emerging CO_2 was continuously collected with a liquid-N_2 cooled trap and subsequently cryogenically cleaned (separation of volatile gases from this trap at liquid nitrogen temperature). Subsequently, water was separated from the remaining gas using a dry-ice ethanol cooled glass trap. The water-free CO_2 gas was then passively passed through silver wool and another trap filled with Porapak Q and held at -35 °C (transit time 33 min). The cleaned CO_2 gas was analyzed immediately or within a few hours.

Mass spectrometric measurements were performed on a Thermo Scientific MAT 253 Plus with a baseline monitoring cup on m/z 47.5 and $10^{13}\Omega$ resistors on m/z 47-49. The analysis protocol consisted of 8 acquisitions with 10 cycles each and an integration time for each cycle of 26 s. Each acquisition included a peak center, background measurements and an automatic bellows pressure adjustment aimed at a 6 V

signal at mass 44. The first acquisition additionally included a recording of the sample m/z 18 (water vapor residual) and m/z 40 signal (Ar – indicator for air remainder). For each cycle the baseline signal on m/z 47.5 was measured simultaneously to the actual sample and reference gas analysis on m/z 44-49. For pressure-baseline (PBL) correction high-voltage peak scans were manually taken at the beginning and/or end of a measurement run. The sample gas was measured against an in-house reference gas standard (Oberlahnstein: $\delta^{13}C$ = -4.42 ‰ VPDB, $\delta^{18}O$ = -9.79 ‰ VPDB). For establishing an absolute reference frame and for interlaboratory comparability, we regularly analyzed community-wide distributed carbonates (ETH1-4, Meckler et al., 2014), Carrara Marble and equilibrated gases (5°C, 25°C, 90°C).
All data were evaluated using a custom-written R script that includes an automatic PBL correction, taking into account that the signal on m/z 47 is additionally influenced by a negative background potentially induced by secondary electrons and broadening of the m/z 44 peak (He et al., 2012; Bernasconi et al., 2013; Fiebig et al., 2015).The empirical transfer function (ETF) was determined based on PBL-corrected Δ_{47} values and uses carbonate standards and equilibrated gases with agreed Δ_{47} values as reference (Dennis et al., 2011). Updated isotope parameters following Daëron et al. (2016) were used for the evaluation.

5.5. Data correction clumped isotopes and fluid inclusions

a) Clumped isotopes

Speleothem calcite isotopes may be influenced by disequilibrium effects. Δ_{47} values are sensitive recorders of kinetic or disequilibrium effects and can be used to assess its magnitude via the difference from the equilibrium Δ_{47} value that is solely determined by temperature (Kluge and Affek, 2012). Disequilibrium in Δ_{47} and $\delta^{18}O$ seems to be linked and leads to a co-variation that is at least consistent at specific cave sites or experimental setups (Daëron et al., 2011; Kluge et al., 2013). Deviations to smaller Δ_{47} values and apparently too high temperatures indicate disequilibrium due to evolution of the mineral-precipitating solution on top of the stalagmite (Hansen et al., 2019) related to prior carbonate precipitation and/or CO_2 degassing (Guo, 2020). The knowledge of the disequilibrium in Δ_{47}, thus, provides also the disequilibrium in calcite $\delta^{18}O$ via the Δ_{47}-$\delta^{18}O$ co-variation slope and allows for its correction (Appendix S1), complementing thus Hendy tests (Daeron et al., 2011; Kluge and Affek, 2012; Kluge et al., 2013). The Δ_{47}-$\delta^{18}O$ correction as outlined in Kluge et al. (2013) for paleo-drip water $\delta^{18}O$ determination is used based on independent paleo-temperature estimates from Emeis et al. (2003) for the EM Sea surface and scaled to the cave location. Together with the Δ_{47}-$\delta^{18}O$ co-variation slope of -0.047 ‰/‰ of Kluge et al. (2013), the observed disequilibrium in Δ_{47} is transferred into calcite $\delta^{18}O$ offsets.

b) Fluid inclusion isotope ratios

Fluid inclusions are robust archives for paleowater and can be used to calculate the calcite formation temperature from the fractionation $^{18}\varepsilon_{calcite\text{-}water}$. We determined the temperature from $^{18}\varepsilon_{calcite\text{-}water}$ with the kinetic-corrected calcite $\delta^{18}O$ (using Δ_{47}; Supplementary S1) and the fluid inclusion $\delta^{18}O$, applying the experimental calibration of Kim and O'Neil (1997) for $^{18}\varepsilon_{calcite\text{-}water}$. However, for some samples additional effects need to be considered. Seasonal or temporary drying of the stalagmite surface can significantly increase water $\delta^{18}O$ and $\delta^{2}H$ values before full fluid inclusion close-off. The fluid $\delta^{18}O$ value could therefore be out of equilibrium with the surrounding calcite that was precipitated earlier from the non-evaporated fluid. Evaporative influence becomes visible if isotope ratios significantly deviate from the Meteoric Water Line (following an evaporation line towards higher $\delta^{18}O$; Weißbach, 2020; Supplementary S3). We assessed the measured fluid inclusion $\delta^{18}O$ values for evaporative effects by comparison with the Mediterranean Meteoric Water Line (MMWL). Note that the MMWL as reference line for the infiltrating karst water may not be fully adequate during glacial periods. McGarry et al. (2004) noted a shift towards the GWML in their fluid inclusion isotope study for some glacial samples. Some of the glacial samples in our study are close to the GWML. Note, however, that the related $^{18}\varepsilon_{calcite\text{-}water}$ of those samples correspond to an unrealistically high nominal temperature (Table 4), indicating that effects other than a shift in the meteoric water line (e.g., evaporation; Weißbach, 2020), may explain the deviation from the MMWL. Thus, our approach of using the MMWL as reference is a first-order

approach for separating fluid inclusions with likely undisturbed meteoric signal from samples influenced by evaporation.

6- Results

6.1. Chronology

25 Uranium/Thorium ages were obtained from the stalagmite Penta-1 (Parts A and B) and Penta-2 (Part C) (Table 1). The age distribution based on the COPRA age model indicates that the stalagmite Penta 2 grew from ca. 174.3 ± 0.6 to 163.4 ± 0.9 ka with a constantly decreasing growth rate (Fig 3). Penta-1 grew from 140.9 ± 0.4 to 112.2 ± 0.5 ka including two discontinuities. One noteworthy hiatus or period with a much lower growth rate from 132.2 ± 0.4 to 127.1 ± 0.5, corresponds to discontinuity D2. The discontinuity D1 covering the period 139.9 ± 0.6 to 137.8 ± 0.6 ka was not investigated further due to stratigraphical disturbances between the 2 adjacent stalagmites. In the upper part of Penta-1 (Segment A), dated between ~127 and ~112 ka, the age model, that was constructed with 8 ages (Fig. 3) displays two distinct periods of relatively constant growth rates: an upper part from 40 mm to top with a lower growth rate of less than 8 mm/ka and the part from 270 to 40 mm with a growth rate of 24 to 217 mm/ka. The lower part of Penta-1 (segment B) covers from 140.9 ± 0.5 ka to 132.2 ± 0.4 up to the second discontinuity D2. All ages in Penta-2 (segment C) are in good stratigraphic order and were used in the calculation of the age model.

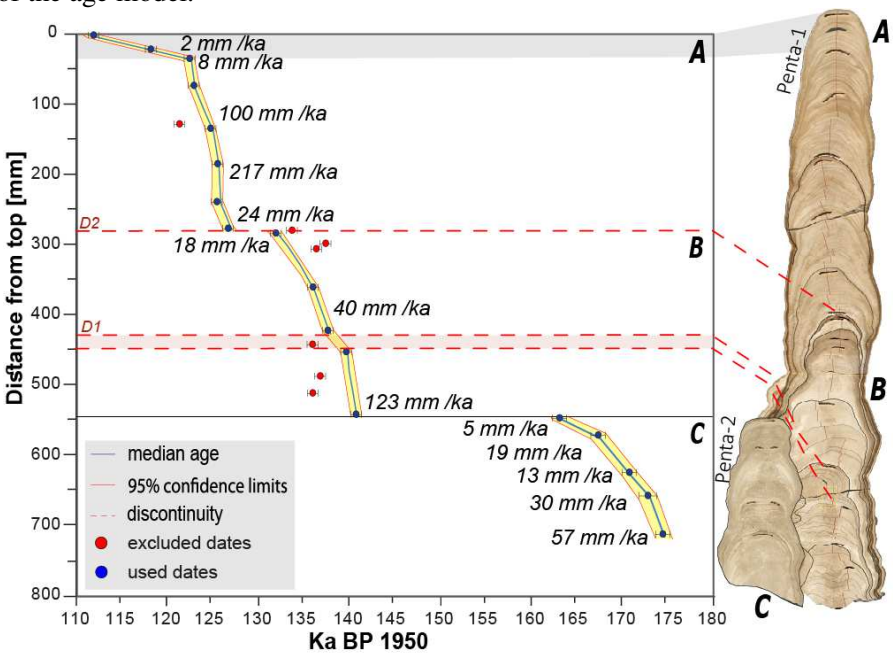

Figure 3. *Age model of the Pentadactylos record. Growth rate of the stalagmite is given next to the age model using COPRA polynomial statistics model between two consecutive dates.*

6.2. Stable isotopic composition of calcite

The $\delta^{18}O$ (–3.3‰ to –9.2‰) and $\delta^{13}C$ values (–4.2‰ to –12.6‰) (Fig. 4) of the Pentadactylos stalagmite roughly display distinct signatures corresponding to the three segments A, B and C as determined based on the sedimentological profile with segments A (from ~110 to ~127 ka) and C (from ~163 to ~174 ka) showing relatively lower $\delta^{18}O$ and $\delta^{13}C$ values than segment B (from 132 ka to 141 ka). The overall resolution of the isotope record is multi-annual (3 to 9 a/mm) to multi-decadal (15 to 60 a/mm), except for the top most part (from ~122 to ~112 ka), which is at lower resolution (270 a/mm). Secondary centennial negative $\delta^{18}O$ excursions of 2 to 3‰, as for example at ~170 ka or ~165 ka (Fig. 4) are observed, mainly in segment C, while $\delta^{13}C$ values are varying rather smoothly on a millennial scale without important centennial excursions.

The $\delta^{13}C$ values generally co-vary, at millennial scale, with the $\delta^{18}O$ values. Growth rate generally vary simultaneously with the $\delta^{18}O$ but especially with the $\delta^{13}C$ values (Fig. 4). A high growth rate generally corresponds to more negative $\delta^{18}O$ and $\delta^{13}C$ values. Noteworthy are the two growth rate peaks at ~126 and ~123 ka occurring together with more negative $\delta^{18}C$ values. After ~122 ka, the growth rate decreases drastically to the top of segment A coeval with a slowly increasing trend in $\delta^{18}O$ and $\delta^{13}C$ values.
Hendy tests (Hendy, 1971) performed along twelve different growth layers show a variation of less than 0.5‰ for $\delta^{18}O$ values and not more than 1‰ for $\delta^{13}C$ values, without clear covariation (Appendix S3). A potential exception could be the samples at 3 cm and 33 cm from top. Thus, kinetic isotope effect cannot be completely excluded but likely have not overprinted important isotopic changes (cf. section 4.4).

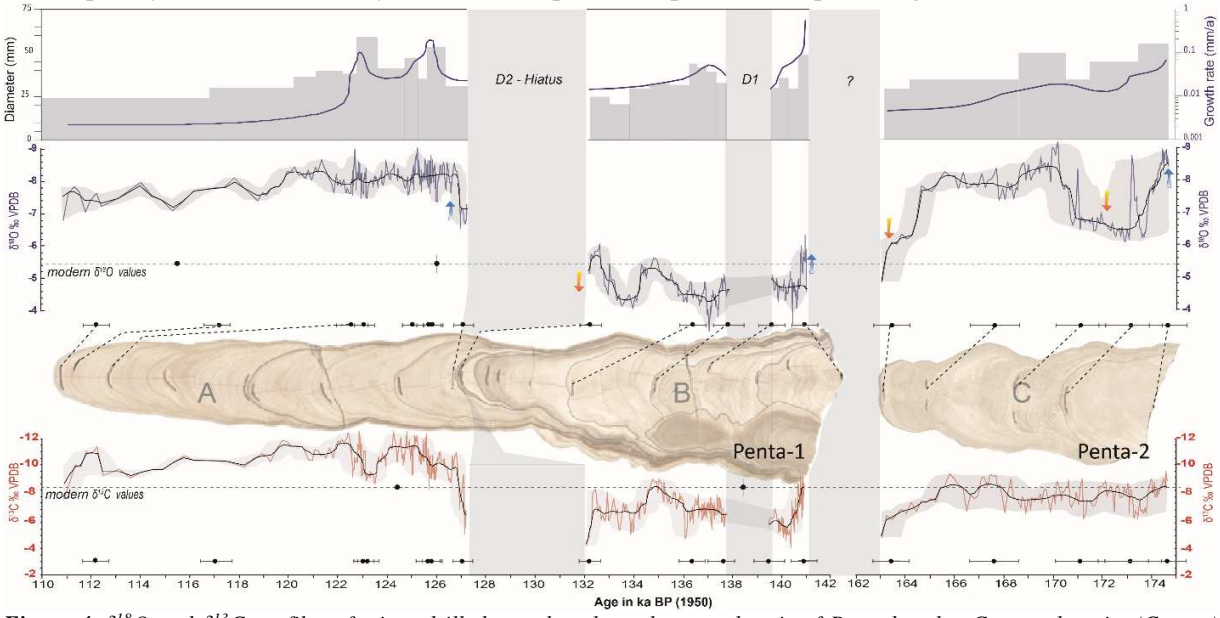

Figure 4. *$\delta^{18}O$ and $\delta^{13}C$ profiles of micro-drilled samples along the growth axis of Pentadactylos Cave stalagmite (Cyprus) reported with their radiometric age. The original isotopic data are presented with their moving average (black line) to clearly show the general trend in isotopic variations from 163 to 174 ka (Penta-2) and from 112 to 141 ka (Penta-1). The period from 138 to 140 ka is not displayed as no isotopic measurements were made for this period. The isotopic changes are displayed relative to V-PDB (Vienna Pee Dee belemnite) together with growth rate (mm/a) and stalagmite diameter (mm). The modern $\delta^{18}O$ and $\delta^{13}C$ values represent calcite samples retrieved under active seepage water from the cave. Blue arrows show wet phases and yellow arrows refer to dry phases.*

6.3. Stable isotopic composition of modern water and calcite fluid inclusions

The average fluid inclusion value is -4.9‰ for $\delta^{18}O_w$ and -26.5‰ for $\delta^{2}H_w$. Replicate analysis shows consistent results at each level, except for the Penta 1-1 samples (56.1 cm from top, 140.9 ka). During MIS6e, $\delta^{18}O_w$ varies between ~-6.0‰ and -1.5‰, with least negative values at the end of MIS6 (140.9 ka). At 137.1 ka, more negative values are set around -4.0‰, leading up to the most negative values during MIS5e: -4.8‰ at 127.0 ka and reaching -8.6‰ at 126.7 ka and -6.8‰ at 125.6 ka. The $\delta^{2}H_w$ values vary between -12 ‰ and -30 ‰ during MIS6 and TII, whereas $\delta^{2}H_w$ values shift to ~-45.0 ‰ at ~126 ka (Table 2). On a comparative basis, present cave and spring water were sampled in December 2018 along the Kyrenian mountain range with -6.6‰ for $\delta^{18}O_w$ and -32.9‰ for $\delta^{2}H_w$. There is a general trend towards more negative $\delta^{18}O_w$ in spring and drip water with increasing altitude from the northern coast to the Kyrenia summits. From the 21 fluid inclusions samples measured, 4 results are considered outliers. Fi-Penta1_1c; Fi_Penta1_3b and Fi_Penta1_8a gave insufficient water (below 0.3µl/g; Table 2) for reliable analysis. Fi-Penta1_1a is related to calcite that was taken at the outer flank of the stalagmite and may therefore be biased due to evaporative enrichment along the flow path.

Table 2. *Pentadactylos fluid inclusions samples in chronological order (old to young) in comparison with modern cave drip and spring water (bottom table). Measurements with an (*) are considered outliers.*

Sample ID	cm/top	U-Th age (ka)	δ^2H_w [‰]	1σ error [‰]	$\delta^{18}O_w$ [‰]	1σ error [‰]	volume [µl]	mass [g]	Water amount [µl/g]
Fluid inclusions									
F1_Penta2_2a	17.5	174.5	-24.39	1.5	-5.43	0.5	2.26	0.41	5.52
F1_Penta2_2b			-26.14	1.5	-5.46	0.5	0.83	0.41	2.02
F1_Penta2_2t			-27.10	1.5	-5.91	0.5	1.14	0.30	3.79
F1_Penta2_4a	10	170.4	-29.81	1.5	-5.97	0.5	0.74	0.31	2.37
F1_Penta2_4b			-27.61	1.5	-5.67	0.5	1.26	0.34	3.70
F1_Penta2_5a	1	163.9	-16.88	1.5	-3.72	0.5	1.45	0.30	4.84
F1_Penta2_5b			-17.12	1.5	-3.86	0.5	0.84	0.24	3.48
F1_Penta1_1c*	56.1	140.9	-19.74	1.5	-3.77	0.5	0.23	0.30	0.78
F1_Penta1_1a*			-20.57	1.5	-6.19	0.5	0.77	0.54	1.43
F1_Penta1_1b			-12.64	1.5	-1.79	0.5	0.78	0.48	1.62
F1_Penta1_1d			-11.36	1.5	-1.61	0.5	0.69	0.47	1.46
F1_Penta1_1t			-20.94	1.5	-4.02	0.5	0.43	0.30	1.42
F1_Penta1_6a	40.5	137.1	-20.54	1.5	-3.60	0.5	0.31	0.28	1.11
F1_Penta1_6b			-21.39	1.5	-4.50	0.5	0.68	0.50	1.37
F1_Penta1_9a	27.2	126.9	-25.43	1.5	-4.83	0.5	0.65	0.31	2.11
F1_Penta1_9c			-24.59	1.5	-4.78	0.5	0.77	0.30	2.57
F1_Penta1_7b	26	126.7	-45.45	1.5	-9.04	0.5	0.64	0.30	2.12
F1_Penta1_7d			-38.86	1.5	-8.29	0.5	0.58	0.33	1.75
F1_Penta1_3b*	14	125.6	-48.47	1.5	-4.86	0.5	0.17	0.31	0.55
F1_Penta1_3t			-43.91	1.5	-6.81	0.5	0.31	0.31	1.00
F1_Penta1_8a*	3	117	-43.99	1.5	-4.32	0.5	0.27	0.32	0.84
Modern cave & spring waters	***altitude (m asl)***								
Smoky cave (mix pool & drip)		756	-20.29	1	-5.24	0.1			
Hot cave_1 (drip)		611	-36.49	1	-7.31	0.1			
Hot cave_2 (drip)		611	-39.51	1	-7.58	0.1			
Kalga spring		505	-33.97	1	-6.67	0.1			
Karagaac spring		289	-32.52	1	-6.51	0.1			
K.Evenkous spring			-35.30	1	-7.08	0.1			
Lepta spring (in-situ)		91	-34.77	1	-6.66	0.1			
Sulfur spring		25	-27.77	1	-5.28	0.1			

6.4. Clumped isotopes

Clumped isotope analysis of the four samples yielded apparent temperatures of 24-29°C (using the Δ_{47}-T relationship of Kluge et al., 2015) that are well above the current cave temperature of 15°C (Table 3), suggesting significant kinetic effects. Offsets of Δ_{47}-related temperatures of 10-15°C are within the range of previous studies (e.g., Daëron et al., 2011; Kluge and Affek, 2012; Kluge et al., 2013; Affek et al., 2014). Following the method outlined in section 5.5, the correction for the kinetic contribution is completed with an effect on the calcite $\delta^{18}O$ value of +0.4-0.9 ‰. The kinetic correction of the calcite $\delta^{18}O$ value is relatively insensitive to the cave paleo-temperature estimates. A deviation of 3°C would change the kinetic $\delta^{18}O$ correction by a maximum of 0.2‰.

Drip water $\delta^{18}O$ values that are related to the formation of the corresponding growth layer were calculated from the corrected calcite $\delta^{18}O$ and an independent temperature estimate. These were scaled to cave temperatures from Sea Surface temperature (SST) of Emeis et al., (2003): 14, 9, 13 and 16.7°C for 126.7, 137, 170.4, and 125.6 ka, respectively. The reconstructed water $\delta^{18}O$ values range from -6.6 to -9.4 ‰ (Table 3) using the oxygen isotope fractionation factor of Kim and O'Neil (1997). These values are similar or more negative than the modern dripwater values (Table 2).

6.5 Paleotemperatures

Paleotemperature calculation is based on the fractionation $^{18}\varepsilon_{calcite\text{-}water}$ using the kinetic-corrected calcite $\delta^{18}O$ (using Δ_{47}) and the fluid inclusion $\delta^{18}O$ (section 5.5 and Appendix S1). $^{18}\varepsilon_{calcite\text{-}water}$ is then converted into temperature applying the experimental calibration of Kim and O'Neil (1997). Calculated temperatures from $^{18}\varepsilon_{calcite\text{-}water}$ range from 14.7 ± 2.7°C to 30.6 ±2.7°C (Table 3). Warmest temperatures are obtained for ~170 ka and ~126 ka, while coldest values are obtained for ~127-141 ka. In contrast to mid- and high latitudes, inclusion $\delta^{18}O_w$ and δD_w cannot be used for direct temperature calculation in the

Mediterranean due to an inconsistent or only weak relationship of mean annual rainfall $\delta^{18}O$ and temperature.

Table 3: *Pentadactylos clumped isotope samples in chronological order (old to young). Calcite powder was retrieved from the remaining powder of the fluid inclusion analysis. The apparent T is based on the Δ_{47}-T calibration of Kluge et al. (2015). n refers to the number of replicates measured per sample. 4b refers to Penta 2, 6b,7b and 3 to Penta 1. The paleotemperature related to each sample was calculated based on $^{18}\varepsilon_{calcite\text{-}fluid}$ following Kim and O'Neil (1997), including corrections for kinetics based on the clumped isotope (see section 5.5 and appendix S1). Uncertainties are based on analytical uncertainties ($\delta^{13}C$, $\delta^{18}O$, Δ_{47}) or Gaussian error propagation (calculated dripwater $\delta^{18}O$ and reconstructed paleotemperature).*

Sample ID	cm from top	U/Th age (ka)	δ^{13}Ccc (‰)	δ^{18}Occ (‰)	Δ_{47} (‰)	Apparent Δ_{47}-T (°C)	Calc $\delta^{18}O_{drip}$ (‰)	T (°C) from $^{18}\varepsilon_{calcite\text{-}water}$	n
4b	10 - Penta 2	170.4	-7.1 ± 0.1	-7.7 ± 0.1	0.700 ± 0.007	24 ± 2	-8.5 ± 0.3	25.5 ± 2.8	3
6b	40.5 - Penta 1	137.1	-7.18 ± 0.02	-4.68 ± 0.04	0.701 ± 0.011	23.5 ± 4	-6.6 ± 0.4	17.2 ± 2.7	2
7b	26 - Penta 1	126.7	-9.5 ± 0.1	-8.5 ± 0.1	0.686 ± 0.017	29 ± 6	-9.4 ± 0.5	14.7 ± 2.4	3
3	14 - Penta 1	125.6	-10.67 ± 0.03	-8.6 ± 0.2	0.699 ± 0.004	24 ± 1	-8.4 ± 0.3	Offset from MMWL	3

7- Discussion

7.1. Age model

COPRA succeeded to produce a coherent age model, although in total seven points out of twenty-five were considered as outliers. A few minor age inversions in growth phases with porous stalagmite parts (Table 1) may be explained by a minor degree of open system behavior. In contrast, there are no indications of detrital Th. Petrographical observation shows that section B (base of Penta 1) is the most porous part of the whole record and where most of the age inversions occurs (Fig. 2). Porous calcite structures are known to be subject of U–Th open-system behavior (Richards and Dorale, 2003; Borsato et al., 2005) *via* dissolution and recrystallization processes of the primary carbonate (Frisia, 2015), remobilization, or post-depositional filling of pores (Schwarcz, 1989), resulting in out-of-sequence ages. Dating points Pentad-2, -5, -14 and Pentad-18 were therefore excluded from the age model. Pentad-19 and 17 are closest to the D2 and D1 respectively, showing stratigraphic perturbations with porous structures and were therefore discarded.

The age model reveals a rather continuous speleothem deposition with two hiatuses in agreement with the observed discontinuities. Two growth stops are noted from ~163 to ~141 ka and from ~132 to ~128 ka. The first growth stop covering the mid-to late penultimate glacial, although consistent generally with a dry period, corresponds to a time gap between the two adjacent stalagmites Penta 1 and Penta-2. The stop in growth may be related to a real climatic deterioration or to a local perturbation in the water routing finally leading to the deposition of the second stalagmite adjacent to the first one. Without replication by a second stalagmite to confirm the cause for this growth stop, one must remain cautious on the possible reasons for this growth interruption. The second growth stop in Penta-1 stalagmite, from ~132 to ~128 ka, corresponds to the discontinuity D2 and is considered as hiatus or period with a much lower growth rate. The discontinuity D1 from 139 to 137 ka is clearly due to the stratigraphical disturbances of the interface between the 2 adjacent stalagmites and is therefore not considered as a hiatus.

7.2. General climatic conditions of the last Glacial/Interglacial cycle in Cyprus

The isotope values of both stalagmites (Fig. 5) roughly suggest three 'climate-related regimes: i) less negative $\delta^{13}C$ (~-8‰) and negative $\delta^{18}O$ values (~-8‰) during the early-penultimate Glaciation (with exception for 173-170 ka and after 165 ka), ii) comparatively less negative $\delta^{13}C$ (~-6‰) and $\delta^{18}O$ values (~-5‰) during the late-penultimate Glaciation and iii) negative $\delta^{13}C$ (~-11‰) and $\delta^{18}O$ values (~-8‰) during the last interglacial period.

During the early-penultimate Glacial, despite large $\delta^{18}O$ variations (~-9.0‰ to ~-5.0‰), $\delta^{13}C$ values remained almost constant around -8‰ (Fig.6), suggesting a Mediterranean vegetation of C3 mixed with C4 type, or the dominance of a C3 type vegetation under water stress due to colder temperatures and/or reduced rainfall as previously suggested for speleothems growth during glacial cycles (Bar-Matthews et al., 2019). However, the quite negative $\delta^{18}O$ values (avg. -8‰) suggest rather wet conditions, supported

by a higher growth rate at the onset of Penta-2 growth. The stalagmite grew continuously until 163 ka, with sufficiently humid conditions to maintain drip water flow in the epikarst zone. After 165 ka, growth rate and stalagmite diameter decreased drastically along with less negative $\delta^{13}C$ and $\delta^{18}O$ values, indicating unfavourable conditions for calcite precipitation. Therefore, the Early-MIS 6 glacial conditions seemed unstable but less severe in Cyprus than the full glacial conditions of the MIS 3/4 period in the Levant (Bar-Matthews et al., 2003; 2019). Speleothem studies from the Soreq, Peqiin, Tzavoa, and Jerusalem Caves and recently form Kanaan cave, Lebanon (Nehme et al., 2018) demonstrated that the climate dynamics from early-penultimate glacial in the EM were unstable with large $\delta^{18}O$ variations. Continuous millennial-scale variabilities extended to the mid-penultimate Glacial and were attributed to D-O like events (Barker et el., 2009) (Fig.6). Climate conditions were relatively cold during the MIS6e, but more humid than the last glacial MIS 3 (Ayalon et al., 2002; Bar-Matthews et al., 2003; Vaks et al., 2006). These findings contradict with those of Cheddadi and Rossignol-Strick (1995), who argued that conditions in the EM during early MIS 6 were very cold and arid, with precipitation below 200 mm, similar to the last two glacial maxima (MIS 4 and 2).

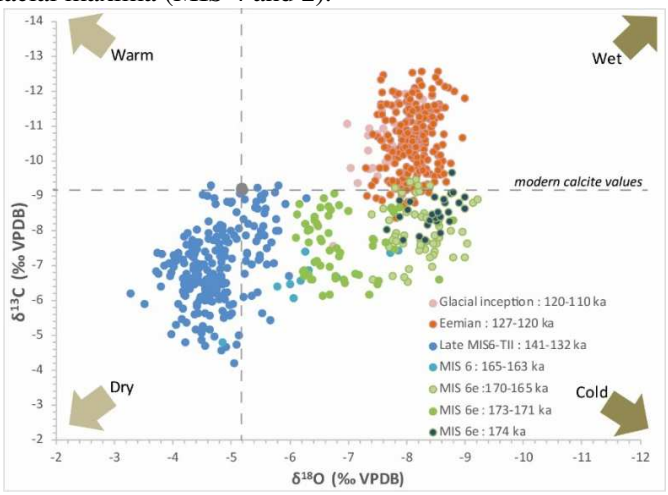

Figure 5. *cross plot of the stable isotope values from Pentadactylos Cave covering the early-MIS 6, the late–MIS 6-TII, the MIS 5e (Eemian), the glacial Inception and modern (late-Holocene) periods. VPDB, Vienna Pee Dee belemnite.*

From 141 to 134 ka, $\delta^{18}O$ and $\delta^{13}C$ values reached the most positive values (Fig. 5) for the entire Pentadactylos record. The average $\delta^{13}C$ value of -6‰ is close to values reached in Soreq and Peqiin caves during the last glacial, with calculated cold temperature of 14-16°C throughout the MIS 4-2 (Affek et al., 2008). Less negative $\delta^{13}C$ in Pentadactylos, potentially caused by a decrease in soil CO_2 concentration, is accompanied by a lower growth rate suggesting lower rainfall amounts or colder temperatures. Similar conditions are noted in the Southern Levant with similar cold and arid climatic conditions in Soreq, Peqiin and Jerusalem records even though with a continuous speleothem growth throughout the entire TII.

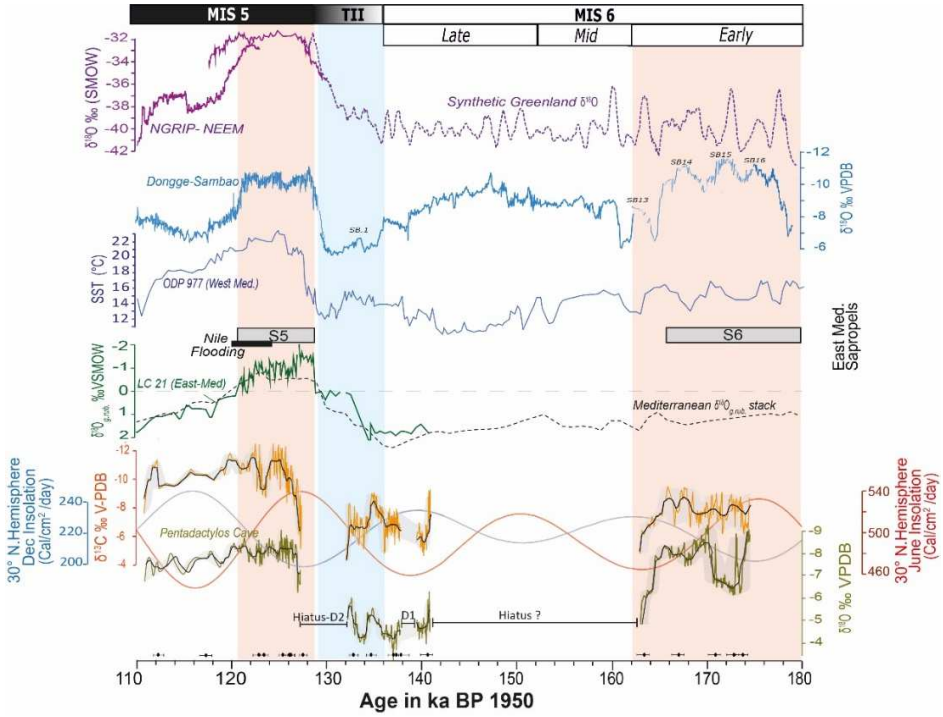

Figure 6. *Marine and global records from 110 to 176 ka excluding the period from 142 to 162 ka (white column) and compared to the Pentadactylos $\delta^{18}O$ profile (this study). Marine and global records comprise $\delta^{18}O$ Greenland ice core (NGRIP, 2004 ; NEEM, 2013) with the synthetic $\delta^{18}O$ record (Barker et al., 2010), Sambao-Dongge $\delta^{18}O$ profile in central China (Wang et al., 2008, Cheng et al., 2016), SST (°C) in ODP 977 marine core (Martrat et al. 2004, 2014), $\delta^{18}O_{g.rub}$ in LC21 marine core (Grant et al., 2012, 2016) and Mediterranean $\delta^{18}O_{g.rub}$ stack (Wang et al., 2010), Sapropels S6 and S5 (Ziegler et al., 2010) and the July insolation at 30° N (Berger and Loutre, 1991).*

The climate conditions during the last Interglacial in Cyprus mark a return to warm and wet conditions with negative $\delta^{18}O$ (-8‰) and $\delta^{13}C$ (-11‰) values starting from ~128 ka (Fig. 6) and supported by the highest growth rates (217 mm/ka) related to a high effective and sustained infiltration in the epikarst. The $\delta^{13}C$ values of ~ −11‰ indicate a significant contribution of soil biogenic CO_2 and thus relatively humid (temperate to warm) conditions. Wet and warm climate conditions were recorded in most of the speleothems of that time period in the Levant basin (Frumkin et al., 2000: Bar-Matthews et al., 2003, Nehme et al., 2015). However, some discrepancies attributed to local and/or regional conditions arise between the records and will be discussed hereafter in section 7.3.

7.3. Climate and $\delta^{18}O$ dynamics from the Pentadactylos record

The penultimate glacial MIS6 conditions, in Cyprus: regional vs local conditions

Between 185 and 135 ka BP, $\delta^{18}O$ values vary between ~ -8‰ and ~-3‰ in the Pentadactylos record while $\delta^{13}C$ remains fairly constant between ~ -8‰ and ~ -6‰ up to ~165 kaAt 175.6 ka, $\delta^{18}O$ values reached -8.8‰ (Fig. 7A) with a moderate growth rate (57 mm/ka), a large stalagmite diameter and the most negative $\delta^{13}C$ signal (~-9.6‰) of MIS 6, in phase with the maximum 30°N June insolation peak (Berger and Loutre, 1991) and a high SST stand (Martrat et al., 2014) (Fig.6). The onset of Penta 2 growth suggests favorable conditions for speleothem growth with active effective recharge, higher drip rate and sufficient contribution of soil biogenic CO_2. Similar conditions are noted in Soreq with more negative $\delta^{18}O$ values from 177 to 174.5 ka (Ayalon et al., 2002). An arboreal pollen (AP%) peak in the Ioannina Basin (Greece) (Roucoux et al., 2011), further supports basin-wide wet conditions (Fig.7A).

From 174 to 171 ka, Pentadactylos shows a positive shift in $\delta^{18}O$ values for ~4 ka, indicating a brief return to drier conditions, coinciding with a positive $\delta^{18}O$ shift at ~174 ka in the Soreq record, albeit longer (3 ka in Penta record vs 8 ka in Soreq record) than in Pentadactylos. From ~170 - 165 ka, a more

532 negative $\delta^{18}O$ value corresponds to the maximum 30° June insolation. It occurs together with a moderate
533 growth rate (19 mm/ka) and is in phase with a gradual increase in the AP% in the Ioannina Basin
534 (Greece). In the southern Levant, the Soreq record displays negative $\delta^{18}O$ values at ~166 ka, slightly later
535 than in Cyprus or Greece. On larger and hemispheric scale, the negative Pentadactylos $\delta^{18}O$ values fall
536 within the large wet intervals identified in Argentarola, Italy (Bard et al., 2002) and Sanbao, China (Wang
537 et al., 2008) (Fig.7A).
538
539 The MIS6e period was known in the EM to be cold and wet (Emeis et al., 2003), during which Sapropel
540 layer S6 is deposited from 178.5 to 165.5 ka (Ziegler et al., 2010). The driver of negative $\delta^{18}O$ values in
541 speleothems would be ascribed to the Mediterranean depleted water source but also to some extent, to
542 enhanced pluvial conditions (amount affect) on land as shown in pollen assemblages in Mediterranean
543 marine records (Cheddadi and Rossignol-Strick, 1995) as well as in the Ioaninna (Roucoux et al., 2011),
544 Greece and Van records (Litt et al., 2014) in North-Eastern Turkey (Fig 7A). An alternative explanation
545 of negative $\delta^{18}O$ values only by temperature changes is rather unlikely, as the observed changes of
546 approximately 2.5‰ at the wet peaks would require a change in temperature of 10-12.5°C, which seems
547 unreasonably high.
548
549 Minor discrepancies between the $\delta^{18}O$ signal in Pentadactylos and other speleothems in the Levant,
550 especially for the 170-165 ka period, lays probably in the local pluvial conditions, which were more
551 intense in the Kyrenia mountains and comparable to pluvial conditions at the Ioannina and Tenaghi-
552 Philippon basins. The persistent and negative $\delta^{13}C$ values from ~175 to 165 ka in Cyprus indicate
553 however a continuous but moderate contribution of soil biogenic CO_2. Speleothem records from the
554 Levant coast (e.g. Soreq, Peqiin, Kanaan) located at lower altitude (<600 m asl) showed $\delta^{13}C$ values more
555 negative than -8‰ for the same period. The $\delta^{13}C$ values exceeding -8‰ in Pentadactylos record can be
556 ascribed to the cave watershed altitude (>800 m asl) showing the altitudinal gradient effect on $\delta^{13}C_{calcite}$
557 (Johnston et al., 2015). After 165.7 ka, a significant change in oxygen and carbon values, growth rate (5
558 mm/ka) and stalagmite diameter point towards unfavorable growth conditions until a growth stop at 163
559 ka along with a clear deterioration of the vegetation cover.

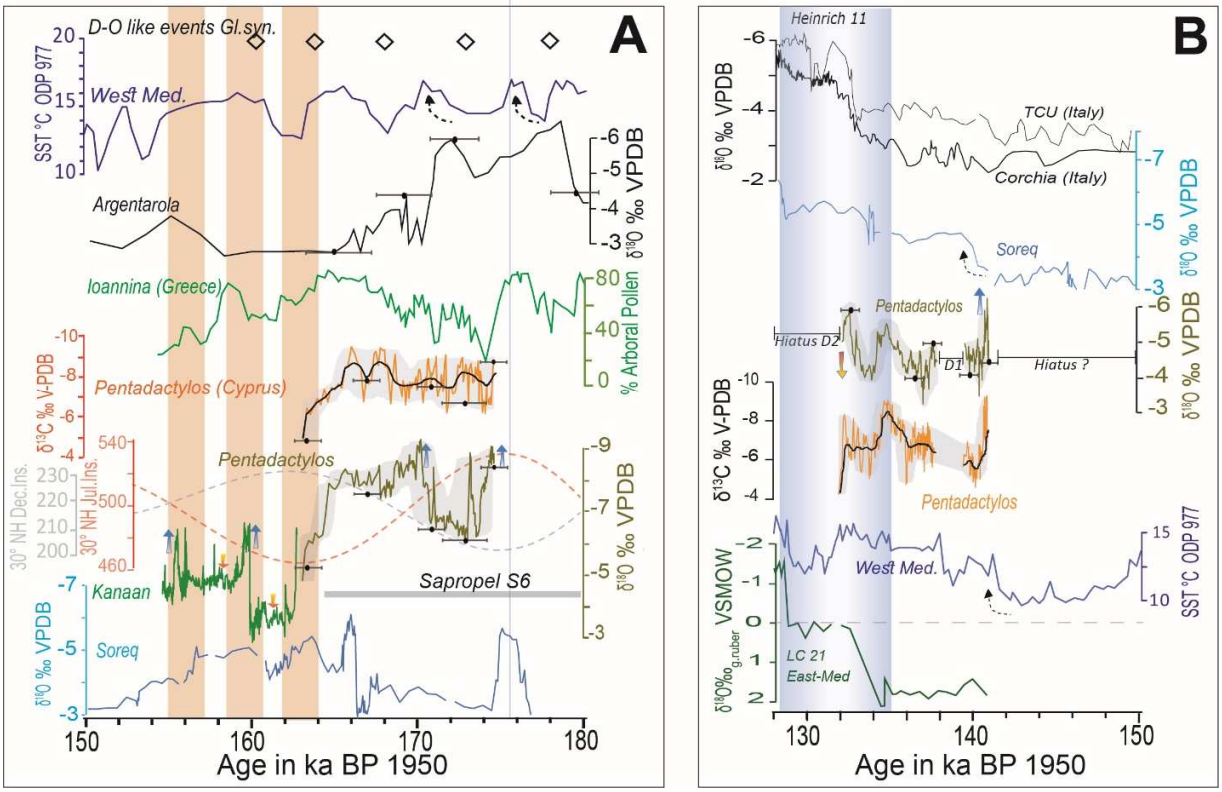

Figure 7. *Paleoclimate records for the penultimate glacial in the Mediterranean basin.* ***A)*** *comparison of the paleoclimate records between 150 and 180 ka showing the Pentadactylos record from 163 to 175 ka (this study) and the U/Th ages with 2σ uncertainty, D-O like events from the Gl.synthetic record (Barker et al., 2009), SST (°C) in ODP 977 marine core (Martrat et al., 2014) the July insolation at 30° N (Berger and Loutre, 1991), $\delta^{18}O$ profile of Argentarola speleothem (Bard et al., 2002), the arboreal pollen (AP) % in the Ionnina basin (Roucoux et al., 2011), Kanaan $\delta^{18}O$ profile (Nehme et al., 2018), Sapropel S6 (Ziegler et al., 2010) and Soreq $\delta^{18}O$ profile (Ayalon et al., 2002; Bar-Matthews et al., 2019). Orange rectangles indicate the Chinese interstadials.* ***B)*** *Comparison of the paleoclimate records between 150 and 130 ka showing the Pentadactylos record from 141 to 132 ka (this study) and the U/Th ages with 2σ uncertainty, TCU (Regattieri et al., 2014) and Corchia (Drysdale et al., 2004, 2009) $\delta^{18}O$ profile, Soreq $\delta^{18}O$ profile (Ayalon et al., 2002; Bar-Matthews et al., 2019), SST (°C) in ODP 977 marine core (Martrat et al., 2014) and $\delta^{18}O_{g.rub}$ in LC21 marine core (Grant et al., 2012). Blue arrows show wetting phase and yellow arrows refer to dry phases.*

The late-penultimate glacial in the Pentadactylos record (Penta 1) includes the period from 141.01 ± 0.56 to 132.25 ± 0.44 ka and part of the Termination (TII), marked by the most less negative $\delta^{18}O$ (avg: -4.6‰) and $\delta^{13}C$ (avg: -7.0‰) values of the entire record (Fig. 6). Overall, climatic conditions were colder (Table 4) and drier than during the early-penultimate period and the record shows a relatively stable maximum glacial state (Fig. 7B). A high growth rate (123 mm/ka) suggests however favorable humid conditions at that time marking a short shift to more effective recharge with the reactivation of calcite growth in Pentadactylos after a long hiatus from 163 to 141 ka. Noteworthy is also the good agreement of Pentadactylos $\delta^{18}O$ with the small negative $\delta^{18}O$ offset in Soreq at ~140 ka. Nonetheless, mild climate conditions prevailed after 140 ka, with lower growth rate (18 mm/ka) and low contribution of soil biogenic CO_2 in Pentadactylos (i.e., less negative $\delta^{13}C$), marking therefore a drier period consistent with an SST lower than 15°C (Martrat et al., 2004) in the Mediterranean Sea and low insolation (Fig. 6). Inland speleothem records show similar climatic trends with less negative $\delta^{18}O$ and $\delta^{13}C$ in TCU, Corchia (Italy) and the Soreq record (Southern Levant).

After 136 ka, two $\delta^{18}O$ negative excursion centered at 134.5 ka and 132.5 ka are noted in the Pentadactylos record. Although the signal at 134.5 ka is not observed or resolved in other records (Fig. 7B), the $\delta^{18}O$ negative peak centered at 132.5 ka agrees within uncertainty with a clear $\delta^{18}O_{g.ruber}$ shift in

LC21 EM marine record (tuned with Soreq chronology) and is concordant with $\delta^{18}O$ negative shift in TCU (Regattieri et al., 2014) and Corchia records. This $\delta^{18}O_{g.ruber}$ negative shift in the Mediterranean basin, prior to the onset of Sapropel S5 (128-120 ka) (Ziegler et al., 2010) has been related to freshwater input to the Mediterranean basin (Rodríguez-Sanz et al., 2017), derived from the North Atlantic source and combined with meltwater discharge from the surrounding mountain ranges (Grant et al., 2016). A source-water control on $\delta^{18}O_{speleothem}$ in southern Italy by the North Atlantic freshwater was also confirmed by Marino et al., (2015) and Tzedakis et al., (2018) for the 135-130 ka period. The $\delta^{18}O$ negative excursions at 134.5 ka and 132.5 ka in Pentadactylos is therefore potentially unrelated to changes in precipitation in Cyprus. At the contrary, a hiatus linked to D2 occurring from 132 to ~128 ka indicates less favourable conditions for speleothem deposition. This period of non-growth is in agreement with the period of lower SST values in the W. Med. marine record and with a positive $\delta^{18}O$ excursion in the TCU (Regattieri et al., 2014) and Dim (Rowe et al., 2020) speleothem record, attributed to a C28 cold event (Oppo et al., 2001) at ~129 ka. Indeed, the non-growth period in the Cypriot speleothem falls within the Heinrich 11 (Heinrich, 1988; McManus et al., 1998), suggesting general cold/dry climate conditions concordant with reduced moisture over the Mediterranean basin.

The G/IG shift in Northern Levant

The last G/IG shift in the EM basin is well-studied in the marine cores as well as in continental records in the southern Levant. In the EM basin, marine $\delta^{18}O_{g.ruber}$ curves (Emeis et al., 2003; Kallel et al., 2000, Rohling et al., 2002; Grant et al., 2012, 2016) display a well-defined orbital modulation of G/IG MIS cycles. Although the marine record follows the global pattern, the $\delta^{18}O_{g.ruber}$ is characterized by larger variations, reaching up to 4.5‰ for the MIS6/5 transition. This large shift reflects the amplification of climate change effects in the EM, due to the contribution of significant inflow of ^{18}O-depleted water during the Sapropel S5 event (128-121 ka ; Ziegler et al., 2010), together with enhanced pluvial conditions in the entire EM basin (Kallel et al., 2000). The effect of the source-water control on $\delta^{18}O_{calcite}$, was largely demonstrated in Southern Levant speleothems for the last G/IG cycle (Bar-Matthews et al., 2019).

The MIS6/5 transition is prominently recorded as a ~5.7‰ shift affecting $\delta^{18}O_{calcite}$ in the Pentadactylos record. This shift is close to Peqiin and Soreq oxygen shifts (5.5 and 5.7‰ respectively) and larger than the amplitude of the $\delta^{18}O_{g.ruber}$ change (source) of the Mediterranean Sea water (Grant et al., 2012) for the last G/IG cycle (Fig. 6). Both Levant and Cypriot speleothem records show a common source of moisture mostly coming from the Mediterranean Levant at the LIG onset. However, the last G/IG amplitude shift in continental records, mostly accounting for the source effect, embed other factors controlling the shift in the $\delta^{18}O_{calcite}$, such as temperature change, rainfall amount, sea-land distance and sea-level. If the seawater $\delta^{18}O_{g.rub}$ shift (4.5‰) accounts for the source effect (Grant et al., 2012) for the MIS 6/5 transition, the remaining 1.2‰ difference would be ascribed for temperature and rainfall amount change in the $\delta^{18}O_{calcite}$ signal of Pentadactylos (Table 4).

The wet and warm Eemian in Cyrpus

The last interglacial in the Pentadactylos stalagmite is recorded at high-resolution from ~127 to ~123 ka. The stalagmite re-started its growth at 127.1 ± 0.5 ka when interglacial conditions were fully attained at the maximum insolation during the Eemian (LIG) period (Fig. 8). A clear negative shift in both $\delta^{18}O$ (avg. -8.03‰) and $\delta^{13}C$ (avg. -10.6‰) curves seems to show a clear vegetation recovery of C3 type with a high contribution of soil biogenic CO_2, combined with enhanced pluvial conditions enough to reactivate effective recharge in a high-altitude epikarst basin (1000 m asl) and to induce the onset of calcite precipitation (growth 24 to 217 mm/ka). The Pentadactylos record shows the highest growth rate (217 mm/ka) at ~126-125 ka. From ~127 to ~123 ka, the record seems to show stable conditions with both negative $\delta^{13}C$ and $\delta^{18}O$ isotope values and high growth rate, indicating favorable warm and wet conditions for speleothem growth, together with developed vegetation cover along the Kyrenia range (Fig. 4).

On the regional scale, these warm and wet conditions in the Kyrenia range fall within longer wet/warm periods identified in the Yammouneh lake record (Develle et al., 2011), the lake Van lacustrine sequence

(Litt et al., 2014), the pollen lacustrine record in southeastern Greece and in Soreq, Peqiin (Ayalon et al., 2002; Bar-Matthews et al., 2003) and Kanaan speleothem records along the Levant coast. The pollen records in the EM basin shows a sharp arboreal pollen increase at the onset of Interglacial 5e (Fig. 8) in agreement with a negative shift in the $\delta^{13}C$ signal of Pentadactylos record. The $\delta^{18}O$ negative shift is also synchronous, within uncertainty, with the Tenaghi-Philipon (Tzedakis et al., 2003, 2009) and Ioaninna pollen records (Roucoux et al., 2011) in Greece, albeit less clear with lake Van, located further East. The particular increase of Sclerophylls pollen in the Greek record, characteristic of Mediterranean woodlands and scrub, indicate a clear regional response to a climate wetting and warming phase.

At ~124-123 ka, a sharp drop in the $\delta^{13}C$ signal lasted 1 ka and coincides with slightly less negative $\delta^{18}O$ values (Fig. 8). This early change in the stable isotope signal could be a response to enhanced seasonality or a modification in moisture source or an early climate deterioration signal with a lower precipitation amount above the Levant basin. This period with low humidity is imprinted in pollen records with a drop in AP % in the Tenaghi-Philippon and Van basins (Fig. 8) at the same time interval, implying thus a regional response to an early climate deterioration.

The Glacial inception in Cyprus vs regional records

The moderate change after 123 ka, with only slightly less negative $\delta^{18}O$ and $\delta^{13}C$ values contrasts with most other speleothem records (Fig.8). Speleothem records along the Levant coast shows drastically less negative $\delta^{18}O$ values after 123 ka, and was interpreted as i) a change towards drier conditions at the onset of the glacial inception period and a reduced contribution of the direct Mediterranean moisture source (Ayalon et al., 2002; Bar-Matthews et al., 2003; Nehme et al., 2015) over the central Levant coast or ii) changes in atmospheric circulation pattern (Kolodny et al., 2005; Lisker et al., 2010). The Kanaan isotopic trend, follows within larger chronological uncertainty the sharp $\delta^{18}O$ drop of Soreq and Peqiin records, reaching significantly less negative values (~4‰) at 122 ka, while the oxygen isotope signal in Cyprus maintains relatively constant negative values after 123 ka, approximately close to ~-7‰ until 110 ka (Fig 8). This clear difference in the stable isotope curves after 123 ka indicate that the Pentadactylos record is closer in amplitude and trend with Corchia and TCU records in northern Italy than the Levant records (Fig 8) when entering the glacial inception.

At the LIG demise, the Pentadactylos record suggests less favourable conditions of growth (8 to 2 mm/ka) and less effective recharge as seen in the drastic growth rate drop after 123 ka (Fig.4). Drier or colder climate conditions might have prevailed from 123 to 110 ka. However, the isotopic values trend in Pentadactylos show a less clear change. Indeed, even if a reduction in the rainfall amount is considered after 123 ka, the $\delta^{18}O$ trend in Cyprus exhibits a clear offset (Fig. 8) from the $\delta^{18}O_{g.rub}$ (source) of the Mediterranean Sea water (Grant et al., 2016), and does not mimic the $\delta^{18}O$ signal of the Levant speleothems, which are mostly source-driven. Pluvial conditions might have been maintained at the LIG demise as shown in the low $\delta^{18}O$ signal by possible distal moisture sources (e.g. North Atlantic), as proposed in studies on rainfall trajectories in the EM realm (Aouad-Rizk et al., 2005; Argiriou and Lykoutis, 2005), with a longer trajectory bringing rainfall with a lighter isotopic signal over the island and extensively over the Northern Levant basin. If the hydrological change at the LIG demise (the glacial inception) between Cyprus and the Levant coast holds true, then the northern Levant basin would be more open to distal and northern rainfall sources under a strong NAO index as noted in the large-scale $\mathbf{\Delta}\delta^{18}O_c$ variability of the Yammouneh record (Northern Lebanon) during glacial intervals (Gasse et al., 2014) as well as in the Jeita record during the LGM period (Cheng et al., 2015).

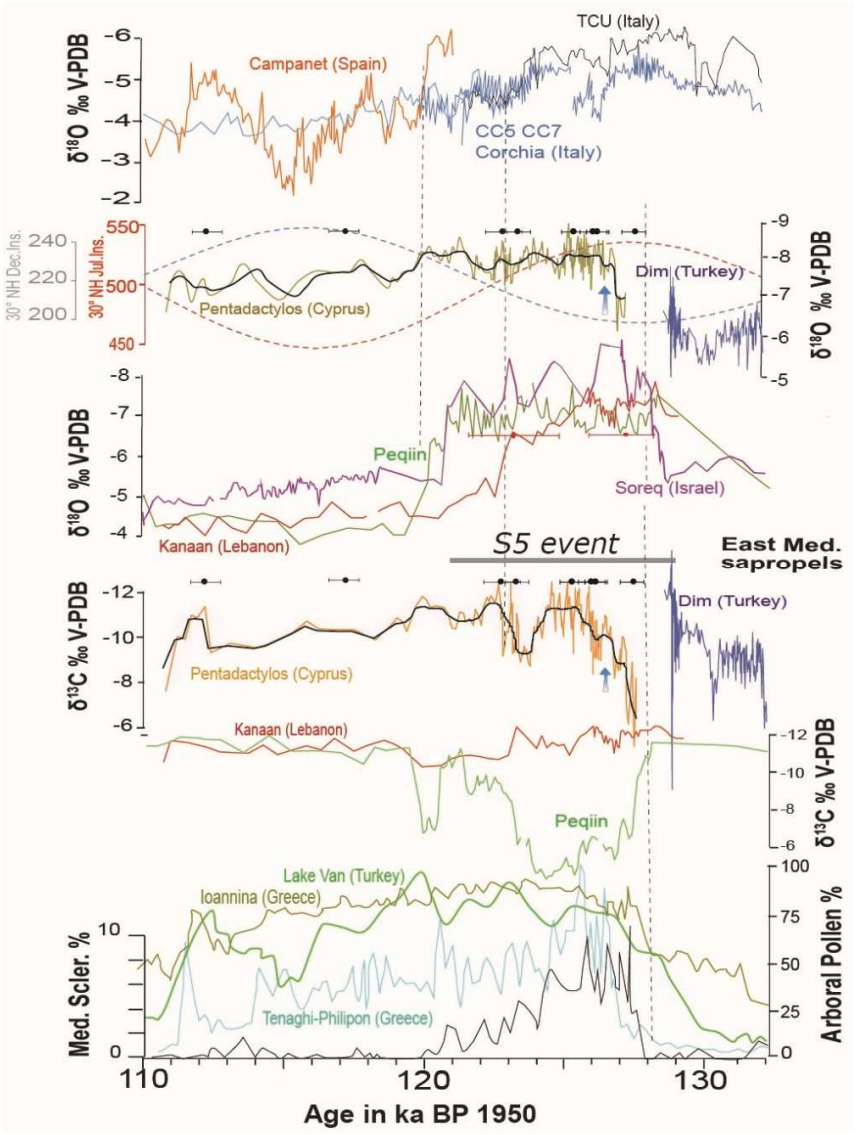

Figure 8. *Paleoclimate records for the penultimate glacial and last Interglacial records in the Mediterranean basin. Continental paleoclimate records from 110 to 134 ka showing TCU and Crochia $\delta^{18}O$ profile (Regattieri et al., 2014; Drysdale et al., 2004, 2009) in northern Italy and Campanet $\delta^{18}O$ profile in Mallorca (Dimitriu et al., 2018), Dim $\delta^{18}O$ and $\delta^{13}C$ profile, Turkey (Rowe et al., 2020), Peqiin and Soreq $\delta^{18}O$ and $\delta^{13}C$ profile (Ayalon et al., 2002, Bar-Matthews et al., 2003), Kanaan $\delta^{18}O$ and $\delta^{13}C$ profile (Nehme et al., 2018), the arboreal pollen (AP) % in Van lake (Litt et al., 2014) and Tenaghi-Philippon (Tzedakis et al., 2004, 2009) and particularly the Mediterranean Sclerophylls pollen in the Ionnina (Tzedakis et al., 2003).*

7.4. Estimates of past temperature and rainfall shifts from MIS 6 to MIS 5

Interpretation of fluid inclusion δD and $\delta^{18}O$

The changes in fluid inclusion δD and $\delta^{18}O$ along the current meteoric waterline with time (Fig. 9) are likely caused by the interplay of three main factors: i) amount effect, ii) source effect and iii) evaporation on the stalagmite top prior to final fluid inclusion close-off. Focusing first on i), the influence of the rainfall amount is exemplified by the most negative δD and $\delta^{18}O$ values at 126.3 and 125.6 ka. This time period has been found to be very wet in the EM (Bar-Matthews et al., 2003; McGarry et al., 2004) pointing towards amount-effect driven changes in the dripwater signal, which results in most negative isotope values in both the Pentadactylos and the Soreq/Pequin/Ma'ale Efrayim data set. Note that the difference of last Interglacial $\delta^{18}O$ values relative to modern drip water $\delta^{18}O$ is comparable for Pentadactylos and Israel (up to -2 ‰).

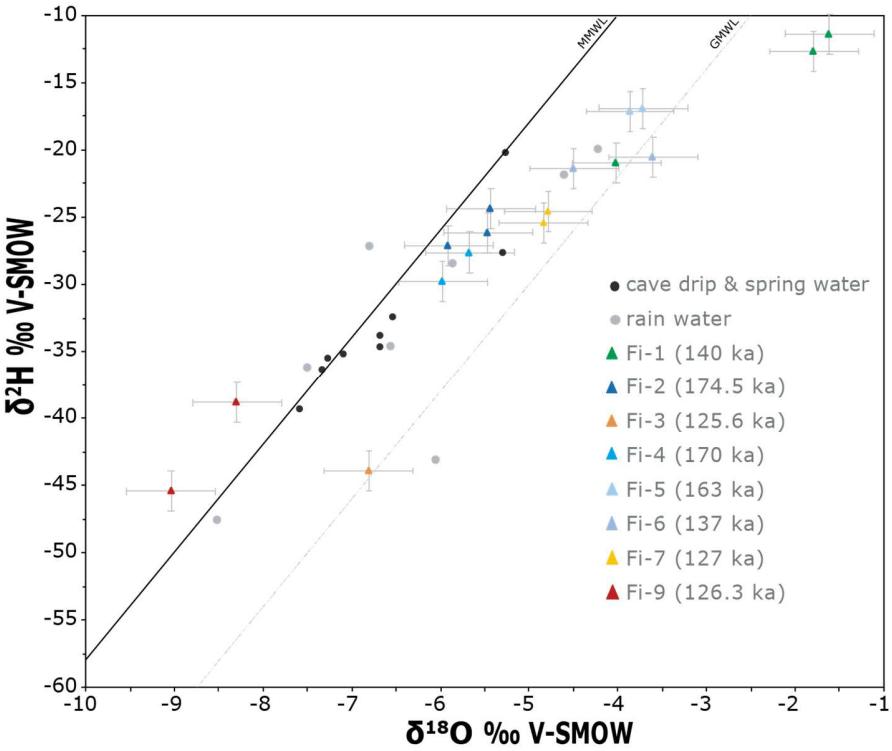

***Figure 9**. $\delta^{18}O$ and $\delta^{2}H$ values of 17 fluid inclusion samples from Pentadactylos stalagmite along with present-day dripwater and stream samples (this study) from the Kyrenia Range and rain water (*IAEA/WMO, 2019*) plotted on the MMWL (Gat et al., 2003) and GMWL (Rozanski et al., 1993).*

Positive $\delta^{18}O$ offsets from the MMWL/GMWL and less negative δD values compared to today, may indicate an influence of evaporation processes. The most positive δD and $\delta^{18}O$ values, with significant offsets from the MMWL or GMWL (Fi-1) suggests an evaporative enrichment in soil and epikarst (Vaks et al., 2003) or significant inner-cave evaporation, both processes taking place preferentially during dry periods. The shifts observed in fluid inclusion $\delta^{18}O$ are up to +6 ‰ relative to modern cave and spring water $\delta^{18}O$ (Table 2) and by far exceed those from equivalent records from Israel for the same time periods (maximum shift: +2 ‰; McGarry et al., 2004). There, glacial samples provided less negative fluid inclusion $\delta^{18}O$ values, closer to the GWML and reflecting a reduced d-excess that may indicate a higher relative humidity. The $\delta^{18}O$ values of McGarry et al. (2004) were calculated from measured fluid inclusion δD and therefore do not reflect the typically strong evaporation effect on $\delta^{18}O$. This can explain the difference to our data set where the positive shift in the measured $\delta^{18}O$ values away from the MMWL cannot solely be explained by a change in the water source isotope values, but also requires an evaporative component (Appendix S3).

Although the amount effect seems to have had a significant influence on the Pentadactylos fluid inclusion $\delta^{18}O$, a determination of paleotemperatures, based on the temperature dependence of the fractionation $^{18}\alpha$ between drip water and calcite is attempted. The temperature dependence of $^{18}\alpha(CaCO_3\text{-}H_2O)$ is known from laboratory experiments or empirical studies and can be used as thermometer. Calculations using the measured fluid inclusion $\delta^{18}O$ and surrounding calcite $\delta^{18}O$ values lead to reasonable temperatures in the range between 14 and 30°C with typical uncertainties of 1-4°C (Fig. 10). However, calculated temperatures for 140 and 160-175 ka appear to be unreasonable, being similar or higher than Interglacial values. An increased influence of evaporative effects during glacial periods as explained previously, may be a likely explanation for this discrepancy. As demonstrated by Verheyden et al. (2008c), low drip rates enable evaporation in caves with increased $\delta^{18}O$ and $\delta^{13}C$ of the subsequent deposited calcite. Moreover, comparing the ε-based temperatures with SSTs (Fig.10) shows that the most reliable reconstructed

temperatures correspond to known wet periods with the lowest speleothems $\delta^{18}O$ values. Therefore, our estimate for the G-IG temperature shift has to be seen as a minimum estimate, with interglacial temperatures close to current values and larger deviations for the glacial samples.

Regional comparison of G-IG temperature shifts

Besides the G-IG temperature shift derived from calcite and fluid inclusion $\delta^{18}O$, the difference in apparent temperature derived from clumped isotopes, also yields a minimum temperature shift of ca.9°C which is of the same order as from the $^{18}\varepsilon_{calcite\text{-}water}$ estimate but smaller than independent estimates from Villars cave speleothems, SW France (Wainer et al., 2011). The authors indicate a shift of 14 ± 2.7° C for the MIS 6 - MIS 5e transition. Noble gas fluid inclusion analyses from a western Germany stalagmite yield 9 ± 5°C (1σ) as a lower bound for temperature rise across TII (Scholz et al., 2009). Other reconstructed temperature data, such as from pollen records from Monticchio Maar in Italy indicate a similar shift with a maximum amplitude of 12°C between the end of MIS 6 and the Last Interglacial optimum (Allen and Huntley, 2009).

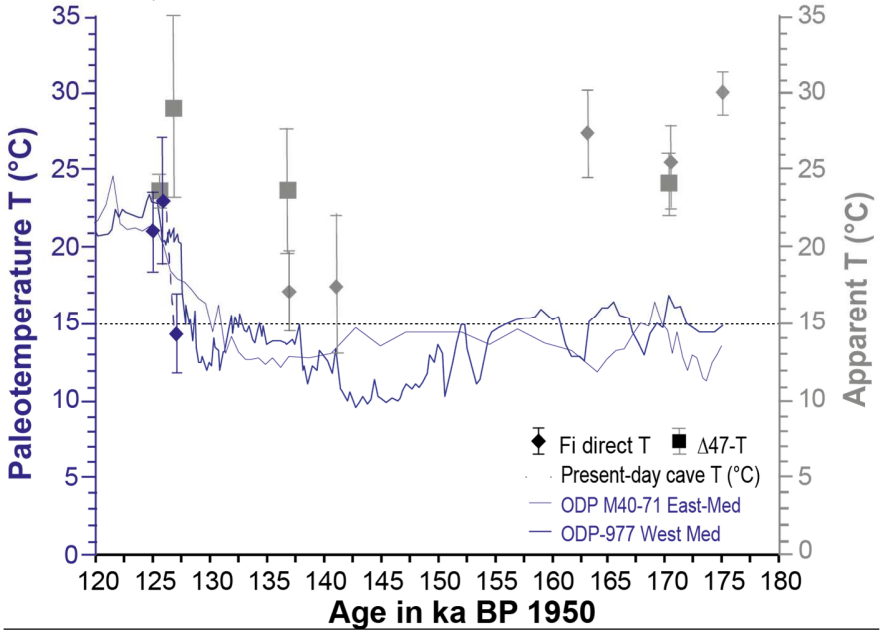

Figure 10. *Paleotemperatures based on the fractionation $^{18}\alpha$(CaCO3-H2O) from fluid inclusion values (in blue) before 130 ka with the apparent T from clumped isotopes analysis (grey squares) based on the Δ_{47}-T calibration of Kluge et al. (2015). Temperatures are plotted against the present-day cave temperature and the SST (blue lines) from the nearby marine cores (M40-71 from Emeis et al., (2003) and ODP-977 from Martrat et al., (2014). Fluid inclusion T that are assumed to be influenced by evaporation are shown as small grey triangles.*

Rainfall amount estimates

Based on the inverse relationship between rainfall $\delta^{18}O$ and precipitation amount in modern observations (IAEA/WMO, 2019; Gat et al., 2003; El-Asrag, 2005; Dirican et al., 2005; Nehme et al., 2019) in the EM, a rainfall increase of ca. 290 mm/a is estimated to relate to a decrease in mean annual rainfall $\delta^{18}O$ of 1‰ (Appendix S2). This value is comparable to the observation of Bar-Matthews et al. (2003) with ca. 200 mm/a per 1‰ at the Soreq cave site. The quantification leads to annual rainfall reconstructions of between <400 and ca. 1200 mm for Cyprus, with peak rainfall during the last interglacial optimum (table 4). Around 170 ka rainfall amounts seem to be <400mm. Rainfall reconstructions for the Last Glacial Period are challenging and not quantitatively attempted here, because little is known on the rainfall $\delta^{18}O$-amount relationship beyond the interglacial conditions.

Table 4. *Temperature T(°C) from $^{18}\varepsilon_{calcite\text{-}fluid}$ after correction for Δ_{47} offset (2nd column) and rainfall amount estimates (3rd column) following an EM relationship between mean annual rainfall $\delta^{18}O$ and amount (Appendix S2). Data were scaled based on modern*

*day rainfall values in Cyprus. *Elevated or high apparent temperatures indicate that an evaporative effect has increased the fluid $\delta^{18}O$ value (*)an evaporative influence may exist. No rainfall amount has been estimated for the full glacial period due to an unknown rainfall amount-$\delta^{18}O$ relationship.*

Age in ka BP	Apparent T (°C)	Estimated precipitation amount (mm)
125.6	20.8 ± 2.5	650 ± 170
126	23.2 ± 4.2	1190 ± 150
127	14.7 ± 2.7	-
137.1	(*)17.2 ± 2.7	-
141	(*)17.6 ± 4.1	-
163.9	*27.6 ± 2.7	-
170.4	*25.5 ± 2.8	370 ± 160
174.5	*30.2 ± 1.4	300 ± 160

8- Conclusion

The Pentadactylos stalagmite record from North-Eastern Cyprus gives new insights into climatic variations during MIS 6 and 5 for the Northern Levant, a region with sparse records spanning the last G/IG cycle. This study suggests moderately temperate and wet conditions in the early MIS6. These conditions prevailed between probably before ~175, to ~163 ka with possibly a short return to dry conditions at ~174ka. The wet period is followed by a stalagmite growth stop, coinciding with the coldest and driest period of MIS 6, from 160 to 141 ka. After 141 ka, slightly more favorable conditions prevail as indicated by slow stalagmite growth. A stop in growth between 132 and 128 ka suggests a short cold and dry period contemporaneous with a Heinrich event.

The onset of the Eemian and along the whole LIG and glacial inception reveal similarities and discrepancies between the Eastern-Mediterranean (EM) records regarding their sensitivity to regional climate. The Pentadactylos $\delta^{18}O$ record was driven mostly by the source effect (Sapropel 5) at the onset of the Eemian, similarly to the Central and Southern Levant sites. Stable conditions during MIS 5e were however rather short in Cyprus compared to Soreq-Peqiin caves located further South. At ~122 ka, a regional climate deterioration is visible in all sites but with different behaviour and isotopic shifts across the glacial inception. A possible change in the regional circulation patterns under a higher NAO index make the northern-Levant more open to distal and northern rainfall sources as noted clearly in the Pentadactylos record situated further North. Other sites along the more Southern coastal Levant would be englobed in the North Atlantic System but remain less influenced than Cyprus, due to the distal locations of these sites.

The estimations of temperature and rainfall amount in Cyprus indicate a temperature shift of ca.9°C at the MIS 6-5 transition and a drastic change in rainfall amount between MIS 6 and 5 (large shift in the measured and calculated fluid inclusion $\delta^{18}O$ value - see Table 2 and 3). The paleotemperature difference estimated from Pentadactylos cave compares well to similar changes in SST for MIS 6 and 5 and confirms the notable marine influence on Cyprus.

9- Acknowledgments

This study is part of the project '*The Caves of Kyrenia Mountains Project: Research, Conservation, and Education'*, supported by the European Union "Cypriot Civil Society in Action V" program (contract number: 2015/371-989) and the US Embassy in Nicosia. Measurements were funded by the IRHIS-60 support grant (University of Rouen-Normandy), the DFG grant KL 2391/2-1 (Germany) and the European Union Civil Society in Action V program. The research was led by Mağara Meraklıları Derneği ("Cave Enthusiasts NGO") in Nicosia, the University of Nicosia, and by the Union Internationale de Spéléologie (UIS). We thank Mustafa Meraklı for abundant logistical support and for guiding us to the entrances of most caves studied here, the Spéléo-club du Liban (SCL) and the Croatian Speleological Federation (HSS) for cooperation in the field and for cave surveying. Many thanks to W.F. Jones and the Bristol Exploration Club (B.E.C.) for their original documentation of Pentadaktylos Pot (Pentadaktylos Cave), and to Dave Gerrard for providing information that allowed the entrance to be re-discovered by the Mağara Meraklıları Derneği team in 2015. Kluge acknowledges support by the Heidelberg Graduate School of Fundamental Physics (DFG-GSC129) and is grateful for support from the research group

"Physics of Environmental Archives" that helped to maintain the IRMS instrument funded through grant DFG-INST 35/1270-1 FUGG.

10- References

Affek H.P., Bar-Matthews M., Ayalon A., Matthews A., Eiler J.M., 2008. Glacial/interglacial temperature variations in Soreq cave speleothems as recorded by 'clumped isotope' thermometry. Geochim. Cosmochim. Ac., 72(22), 5351-5360.

Affek H.P., Matthews A., Ayalon A., Bar-Matthews M., Burstyn Y., Zaarur S., Zilberman T., 2014. Accounting for kinetic isotope effects in Soreq Cave (Israel) speleothems. Geochim. Cosmochim. Ac., 143, 303-318.

Affolter S., Fleitmann D., Leuenberger M., 2014. New-on-line method for water isotope analysis of speleothem fluid inclusions using laser absorption spectroscopy (WS-CRDS). Clim. Past, 10, 1291-1304.

Affolter S., Häuselmann A.D., Fleitmann D., Häuselmann P., Leuenberger M., 2015. Triple isotope (δD, $\delta^{17}O$, $\delta^{18}O$) study on precipitation, drip water and speleothem fluid inclusions for a W.Central European cave (Switzerland), Quat. Sci. Rev. 127, 73-89

Allen, J.R.M. and Huntley, B., 2009. Last Interglacial palaeovegetation, palaeoenvironments and chronology: a new record from Lago Grande di Monticchio, southern Italy. Quat. Sci. Rev. 28, 1521e1538.

Alpert P., Price C., Krichak S.O., Ziv B., Saaroni H., Osetinsky I., Kishcha P., 2005. Tropical teleconnections to the Mediterranean climate and weather. Advances in Geosciences, 2, 157-160.

Aouad-Rizk A., Job J.L., Najem W., Travi Y., Blavoux B., Gourcy L., 2005. Oxygen-18 and deuterium contents over Mount Lebanon related to air mass trajectories and local parameters. IAEA, Isotopic composition of precipitation in the Mediterranean Basin in relation to air circulation patterns and climate, 75-82.

Argiriou, A.A. and Lykoutis S., 2005. Stable isotopes in rainfall over Greece: results of the 2000–2003 measurement campaign. IAEA, Isotopic composition of the precipitation in the Mediterranean Basin in relation to air circulation patterns and climate, Vienna, Austria, 83-98.

Ayalon A., Bar-Matthews M., Kaufman A., 2002. Climatic conditions during marine isotopic stage 6 in the Eastern Mediterranean region as evident from the isotopic composition of speleothems: Soreq Cave, Israel. Geology 30, 303–306.

Ayalon A., Bar-Matthews M., Frumkin A., Matthews A., 2013. Last Glacial warm events on Mount Hermon: the southern extension of the Alpine karst range in the east Mediterranean, Quat. Sci. Rev., 59, 43–56.

Baker A. and Smart P.L., 1995. Recent flowstone growth rates: field measurements in comparison to theoretical predictions, Chem. Geol., 122, 121–128.

Baker A., Genty D., Dreybrodt W., Barnes W.L., Mockler N.J., Grapes J., 1998. Testing theoretically predicted stalagmite growth rate with recent annually laminated samples implication for past stalagmite deposition. Geochim. Cosmochim. Acta 62, 393–404

Bard E., Antonioli F., Silenzi S., 2002. Sea-level during the penultimate interglacial period based on a submerged stalagmite from Argentarola Cave (Italy). Earth Planet Sci. Lett., 196, 135–146.

Barker S., Knorr G., Edwards R.L., Parrenin F., Putnam A.E., Skinner L.C., Wolff E., Ziegler M., 2011. 800,000 years of abrupt climate variability. Science 334, 347–351.

Berger A. and Loutre M.F., 1991. Insolation values for the climate of the last 10 million years. Quat. Sci. Rev., 10, 297–317.

Bar-Matthews M., Ayalon A., Gilmour M., Matthews M., Hawkesworth C., 2003. Sea-land isotopic relationships from planktonic foraminifera and speleothems in the Eastern Mediterranean region and their implications for paleorainfall during interglacial interval. Geochim. Cosmochim. Acta, 67, 3181–3199.

Bar-Matthews M., Keinen J., Ayalon A., 2019. Hydro-climate research of the late quaternary of the Eastern Mediterranean-Levant region based on speleothems research. A review. Quat. Sci. Rev., 221, 105872.

Benetti M., Reverdin G., Pierre C., Merlivat L., Risi C., Steen-Larsen H.C., Vimeux F., 2014. Deuterium excess in marine water vapor: Dependency on relative humidity and surface wind speed during evaporation. J. Geophys. Res. Atmos., 119, 584–593.

Bernasconi S. M., Hu B., Wacker U., Fiebig J., Breitenbach S.F.M, Rutz T., 2013. Background effects on Faraday collectors for clumped isotope measurements. Rapid Commun. Mass Spectrom. 27, 603–612.

Borsato A., Quinif Y., Bini A., Dublyansky Y., 2005. Open system alpine speleothems: implications for U-series dating and paleoclimate reconstructions. Studi Trentini Di Scienze Naturali, Acta Geologica 80, 71–83.

Breitenbach S.F.M., Rehfeld K., Goswami B., Baldini J.U.L., Ridley H.E., Kennett D.J., Prufer K.M., et al., 2012. Constructing proxy records from age models (COPRA). Clim. Past, 8, 1765–1779.

Cailhol D., Audra P., Nehme C., Nader F., Garašić M., Heresanu V., Gucel S., Charalambidou I., Cheng H., Edwards R. L., 2019. The contribution of condensation-corrosion in the morphological evolution of caves in semi-arid regions: preliminary investigations in the Kyrenia range, Cyprus. Acta Carsologica, 48/1, 9-33.

Cheddadi R. and Rossignol-Strick M., 1995. Eastern Mediterranean Quaternary paleoclimates from pollen and isotope records of marine cores in the Nile cone area, Paleoceanography, 10, 291–300.

Cheng H., Zhang P.Z., Spötl C., Edwards R.L., Cai Y.J., Zhang D.Z., Sang W.C., Tan M., An Z.S., 2012. The climatic cyclicity in semiarid-arid central Asia over the past 500,000 years. Geophys. Res. Lett., 39, L01705.

Cheng H., Edwards R.L., Shen C.C., Polyak V.J., Asmerom Y., Woodhead J., Hellstrom J., 2013. Improvements in ^{230}Th dating, ^{230}Th and ^{234}U half-life values, and U–Th isotopic measurements by multi-collector inductively coupled plasma mass spectrometry. Earth Planet Sci. Lett., 371, 82–91.

Cheng, H., Sinha, A., Verheyden, S., Nader, F.H., Li, X.L., Zhang, P.Z., Yin, J.J., Yi, L., Peng, Y.B., Rao, Z.G. and Ning, Y.F., 2015. The climate variability in northern Levant over the past 20,000 years. Geophys. Res. Lett., 42(20), 8641-8650.

Cheng H., Edwards R.L., Sinha A., Spötl C., Yi L., Chen S., Kelly M., Kathayat G., Wang X., Li X., Kong X., Wang Y., Ning Y., Zhang H., 2016. The Asian monsoon over the past 640,000 years and ice age terminations. Nature 534, 640–646.
Columbu A., Drysdale R., Capron E., Woodhead J., De Waele J., Sanna L., Hellstrom J. Bajo P., 2017. Early last glacial intra-interstadial climate variability recorded in a Sardinian speleothem. Quat. Sc. Rev., 169, 391-397.
Columbu A., Spötl C., De Waele J., Yu T.L., Shen C.C., and Gázquez F., 2019. A long record of MIS 7 and MIS 5 climate and environment from a western Mediterranean speleothem (SW Sardinia, Italy). Quat. Sci. Rev., 220, 230-243.
Constantinou, G., 1995. Geological Map of Cyprus, 1/250.000.- Geological Survey of Cyprus.
Daëron M., Guo W., Eiler J., Genty D., Blamart D., Boch, R., Drysdale R.N., Maire R., Wainer K., Zanchetta G., 2011.^{13}C-^{18}O clumping in speleothems: observations from natural caves & precipitation experiments, Geochim. Cosmochim. Acta, 75, 3303–3317.
Daëron M., Blamart D., Peral M., Affek H.P., 2016. Absolute isotopic abundance ratios and the accuracy of Δ_{47} measurements. Chem. Geol. 442, 83–96.
Dennis K.J., Affek H.P., Passey B.H., Schrag D.P., Eiler J.W., 2011. Defining an absolute reference frame for 'clumped' isotope studies of CO_2. Geochim. Cosmochim. Acta 75, 7117–7131.
Develle A.L., Gasse F., Vidal L., Williamson D., Demory F., Van Campo E., Ghaleb B., Thouveny N., 2011. A 250ka sedimentary record from a small karstic lake in the Northern Levant (Yammoûneh, Lebanon): Paleoclimatic implications, Palaeogeogr. Palaeoclim., Palaeoecol., 305, 10–27, 2011
Dumitru O.A., Onac B.P., Polyak V.J., Wynn J.G., Asmerom Y., Fornós J.J., 2018. Climate variability in the western Mediterranean between 121 and 67 ka derived from a Mallorcan speleothem record. Palaeogeogr. Palaeoclim., Palaeoecol., *506*, 128-138.
Dirican A., Unal S., Acar Y., Demircan M., 2005. The temporal and seasonal variation of δ 2H and δ 18O in atmospheric water vapour and precipitation from Ankara, Turkey in relation to air mass trajectories at Med. Basin. In: Isotopic composition of precipitation in the Mediterranean Basin in relation to air circulation patterns and climate. IAEA-TECDOC, 1453: 191-214.
Dutton A. and Lambeck K., 2012. Ice volume and sea level during the last interglacial, Science, 337, 216–219.
Dreybrodt, W., 1988. *Processes in Karst Systems*. Springer, New York.
Dreybrodt W., 1999. Chemical kinetics, speleothem growth and climate. Boreas 28, 347–356.
Drysdale R.N., Zanchetta G., Hellstrom J.C., Fallick A.E., Zhao J.X., Isola I., Bruschi G., 2004. Palaeoclimatic implications of the growth history and stable isotope (δ^{18}O; δ^{13}C) geochemistry of a Middle to Late Pleistocene stalagmite from central western Italy. Earth Planet Sci. Lett, 227, 215–229.
Drysdale R., Hellstrom J., Zanchetta G., Fallick A.E., Sánchez Goñi M.F., Couchoud I., McDonald J., Maas, R., Lohmann, G., and Isola I., 2009. Evidence for obliquity forcing of glacial Termination II, Science, 325, 1527–1531.
Dublyansky Y.V. and Spötl C., 2009. δ^{18}O & δ^{2}H of water from inclusions in minerals: design of a new crushing system and on-line continuous-flow isotope ratio mass spectrometric analysis. Rapid Commun Mass Spectrom, 23(17), 2605-2613.
Duplessy J.C., Labeyrie L., Arnold M., Paterne M., Duprat J., Van Weering T.C.E., 1992. Changes in surface salinity of the North Atlantic Ocean during the last deglaciation. Nature, 358 (6386), 485.
Edwards R.L., Chen J.H., Ku T.L., Wasserburg G.J., 1987. Precise timing of the last interglacial period from mass spectrometric determination of ^{230}Th in corals. Science 236, 1547–1553.
Ehlers J., Gibbard P.L., 2007. The extent and chronology of Cenozoic global glaciation. Quaternary International 164, 6–20.
El-Asrag A.M., 2005. Effect of synoptic and climatic situations on fractionation of stable isotopes in rainwater over Egypt and east Mediterranean. In: Isotopic composition of precipitation in the Mediterranean Basin in relation to air circulation patterns and climate. IAEA TECDOC, 1453: 51-73.
Emeis K.C., Schulz H., Struc U., Rossignol-Strick M., Erlenkeuser H., Howell M.W., Kroon D., 2003. Eastern Mediterranean surface water temperatures and $\boldsymbol{\delta}^{18}$O during deposition of sapropels in the late Quaternary. Paleoceanography 18, 1005–1029.
Fairchild I.J., Smith C.L., Baker A., Fuller L., Spötl C., Mattey D., McDermott F., 2006. Modification and preservation of environmental signals in speleothems. Earth Sci. Rev. 75, 105–153.
Fairchild, I.J. and Baker, A., 2012. *Speleothem science: from process to past environments*, Vol. 3. John Wiley & Sons, 416 pages.
Fiebig J., Hofmann S., Löffler N., Lüdecke T., Methner K., and Wacker U., 2015. Slight pressure imbalances can affect accuracy and precision of dual inlet-based clumped isotope analysis, Isotopes in Environmental and Health Studies.
Frisia S., 2015. Microstratigraphic logging of calcite fabrics in speleothems as tool for paleoclimate studies. Int. J. Speleol. 44, 1–16.
Frumkin A., Ford D.C., Schwarcz H.P., 1999. Continental oxygen isotopic record of the last 170,000 years in Jerusalem, Quat. Res., 51, 317–327,
Frumkin A., Ford D.C., Schwarcz H., 2000. Paleoclimate and vegetation of the Last Glacial cycles in Jerusalem from a speleothem record. Global Biogeochem. Cycles 14, 863–870.
Gat J.R., Klein B., Kushnir Y., Roether W., Wernli H., Yam R., Shemesh A., 2003. Isotope composition of air moisture over the Mediterranean Sea: an index of the air–sea interaction pattern. Tellus, 55(5), 953-965.
Gasse F., Vidal L., Van Campo E., Demory F., Develle A.L., Tachikawa K., Thouveny N., 2014. Hydroclimatic changes in northern Levant over the past 400,000 years. Quat. Sci. Rev., 111, 1-8.
Grant K.M., Rohling E.J., Bar-Matthews M., Ayalon A., Medina-Elizalde M., Bronk-Ramsey C., Satow C., Roberts A.P., 2012. Rapid coupling between ice volume and polar temperature over the past 150 ka, Nature 491, 744–747.
Grant K.M., Grimm R., Mikolajewicz U., Marino G., Ziegler M., Rohling E.J., 2016. The timing of Mediterranean sapropel deposition relative to insolation, sea-level and African monsoon changes. Quat. Sci. Rev., 140, 125-141.

Genty D., Baker A., Vokal B., 2001. Intra- and inter-annual growth rate of modern stalagmites. Chem. Geol., 176, 191–212.
Genty D., Blamart D., Ouahdi R., Gilmour M., 2003. Precise dating of Dansgaard–Oeschger climate oscillations in western Europe from stalagmite data. Nature 421, 833–837.
Genty D., Blamart D., Ghaleb B., Plagnes V., Causse C., Bakalowicz M., Zouari K., et al., 2006. Timing and dynamics of the last deglaciation from European and North African $\delta^{13}C$ stalagmite profiles-comparison with Chinese and South Hemisphere stalagmites. Quat. Sci. Rev., 25, 2118–2142.
Genty D., Labuhn I., Hoffmann G., Danis P.A., Mestre O., Bourges F., Wainer K., Massault M., Van Exter S., Régnier E., Orengo Ph., Falourd S., Minster B., 2014. Rainfall and cave water isotopic relationships in two South-France sites. Geochim. Cosmochim. Acta, 131, 323-343.
Guo W., 2020. Kinetic clumped isotope fractionation in the DIC-H_2O-CO_2 system: patterns, controls, and implications. Geochim. Cosmochim. Acta, 268, 230-257.
Hansen M., Scholz D., Schöne B.R., Spötl C., 2019. Simulating speleothem growth in the laboratory: Determination of the stable isotope fractionation ($\delta^{13}C$, $\delta^{18}O$) between H_2O, DIC and $CaCO_3$. Chem. Geol., 509, 20-44.
He B., Olack G.A., Colman A.S., 2012. Pressure baseline correction and high-precision CO^2 clumped-isotope (Δ_{47}) measurements in bellows and micro-volume modes. Rapid Commun Mass Spectrom. 26, 2837–2853.
Hendy C.H., 1971. The isotopic geochemistry of speleothems – I., The calculation of the effects of different modes of formation on the isotopic composition of speleothems and their applicability as palaeoclimatic indicators, Geochim. Cosmochim. Acta, 35, 801– 824.
Heinrich H., 1988. Origin and consequences of cyclic ice rafting in the northeast Atlantic Ocean during the past 130,000 years. Quat. Res., 29(2), 142-152.
Huntington K.W., Eiler J.M., Affek H.P., Guo W., Bonifacie M., Yeung L.Y., Thiagarajan N., Passey B., Tripati A., Daëron M., Came R., 2009. Methods and limitations of 'clumped' CO2 isotope (Δ_{47}) analysis by gas-source isotope ratio mass spectrometry. J. Mass Spectrom. 44, 1318–1329.
IAEA/WMO, 2019. Global Network of Isotopes in Precipitation. The GNIP Database. Accessible at: http://www.iaea.org/water
Interwies E., Görlitz S., 2012. The role of water pricing and water allocation in agriculture in delivering sustainable water use in Europe – CASE STUDY CYPRUS. InterSus - Sustainability Services. European Commission Project n° 11589. 35 pages.
Jaffey A.H., Flynn K.F., Glendenin L.E., Bentley W.C., Essling A.M., 1971. Precision measurement of half-lives and specific activities of ^{235}U and ^{238}U. Phys. Rev. C4, 1889–1906.
Kallel N., Duplessy J.C., Labeyrie L., Fontugne M., Paterne M., Montacer M., 2000. Mediterranean pluvial periods and sapropel formation over the last 200 000 years. Palaeogeo., Palaeoclim., Palaeoecol. 157 (1), 45–58
Keinan J., Bar-Matthews M., Ayalon A., Zilberman T., Agnon A., Frumkin A., 2019. Paleoclimatology of the Levant from Zalmon Cave speleothems, the northern Jordan Valley, Israel. Quat. Sc. Rev., 220, 142-153.
Kim S.T. and O'Neil J.R., 1997. Equilibrium and nonequilibrium oxygen isotope effects in synthetic carbonates. Geochim., Cosmochim. Acta, 61(16), 3461-3475.
Kiro Y., Goldstein S.L., Garcia-Veigas J., Levy E., Kushnir Y., Stein M., Lazar B., 2017. Relationships between lake-level changes & water & salt budgets in the Dead-Sea during extreme aridities in the East. Mediter. Earth Planet Sci. Lett., 464, 211-226.
Kluge T. and Affek H.P., 2012. Quantifying kinetic fractionation in Bunker Cave speleothems using Δ_{47}.Quat. Sci. Rev. 49, 82–94.
Kluge T., Affek H.P., Marx T., Aeschbach-Hertig W., Riechelmann D.F.C., Scholz D., Riechelmann, S., Immenhauser, A., Richter, D.K., Fohlmeister, J., Wackerbarth, A., Mangini, A., Spötl, C., 2013. Reconstruction of drip-water $\delta^{18}O$ based on calcite oxygen and clumped isotopes of speleothems from Bunker Cave (Germany). Clim. Past, 9(1), 377–391
Kluge T., John C.M., Jourdan A.L., Davis S., Crawshaw J., 2015. Laboratory calibration of the calcium carbonate clumped isotope thermometer in the 25–250°C temperature range. Geochim. Cosmochim Acta, 157, 213-227.
Kluge T., Münster T.S., Frank N., Eiche E., Mertz-Kraus R., Scholz D., Finné M., Unkel I., 2020. A 4000-year long Late Holocene climate record from Hermes Cave (Peloponnese, Greece), Clim. Past Discuss., doi.org/10.5194/cp-2020-47, in review.
Kroon D., Alexander I., Little M., Lourens L.J., Matthewson A., Robertson A.H., Sakamoto T., 1998. Oxygen isotope and sapropel stratigraphy in the eastern Mediterranean during the last 3.2 Ma. Proceedings of the Ocean Drilling Program, Scientific Results, 160, 14.
Kopp R.E., Simons F.J., Mitrovica J.X., Maloof A.C., Oppenheimer M., 2009. Probabilistic assessment of sea level during the last interglacial stage. Nature, 462, 863–867.
Kottek M., Grieser J., Beck C., Rudolf B., Rubel F., 2006. World map of the Köppen-Geiger climate classification updated. Meteorologische Zeitschrift, 15(3), 259-263.
Kolodny Y., Stein M., Machlus M., 2005. Sea–rain–lake relation in the Last Glacial East Mediterranean revealed by $\delta^{18}O$-$\delta^{13}C$ in Lake Lisan aragonites. Geochim. Cosmochim. Acta 69, 4045–4060.
Lachniet, M.S., 2009. Climatic and environmental controls on speleothem $\delta^{18}O$ values. Quat. Sci. Rev., 28(5-6), 412-432.
Lachniet M.S., Bernal J.P., Asmerom Y., Polyak V., 2012. Uranium loss and aragonite–calcite age discordance in a calcitized aragonite stalagmite. Quat. Geochronology, 14, 26–37.
Lisker S., Vaks A., Bar-Matthews M., 2010. Late Pleistocene palaeoclimatic and palaeoenvironmental reconstruction of the Dead Sea area (Israel), based on speleothems and cave stromatolites, Quat. Sci. Rev., 29, 1201–1211.
Litt T., Pickarski N., Heumann G., Stockhecke M., Tzedakis P.C., 2014. A 600,000 year-long continental pollen record from Lake Van, easternAnatoloia (Turkey). Quat. Sci. Rev., 104, 30–41.

Margari V., Skinner L.C., Tzedakis P.C., Ganopolski A., Vautravers M., Shackleton N.J., 2010. The nature of millennial-scale climate variability during the past two glacial periods. Nature Geoscience 3, 127–131.
Martrat B., Grimalt J.O., Lopez-Martinez C., Chaco I., Sierro F.J., Flores J.A., Zahn R., Canals M., Jason H.C., Hodell D.A., 2004. Abrupt temperature changes in the Western Mediterranean over the past 250,000 years. Science 306, 1762–1765.
Martrat B., Jimenez-Amat P., Zahn, R., Grimalt J. O., 2014. Similarities and dissimilarities between the last two deglaciations and interglaciations in the North Atlantic region. Quat. Sci. Rev., 99, 122-134.
Masson-Delmotte V., Schulz M., Abe-Ouchi A., Beer J., Ganopolski A., González Rouco J.F., Osborn T., 2013. Information from paleoclimate archives. 383-464
Matthews A., Ayalon A., Bar-Matthews M., 2000. D/H ratios of fluid inclusions of Soreq cave (Israel) speleothems as a guide to the Eastern Mediterranean Meteoric Line relationships in the last 120 ka. Chem. Geol., 166(3-4), 183-191.
McGarry S., Bar-Matthews M., Matthews A., Vaks A., Schilman B., Ayalon A., 2004. Constraints on hydrological and paleo-temperature variations in the Eastern Mediterranean region in the last 140 ka given by the δD values of speleothem fluid inclusions, Quat. Sci. Rev., 23, 919–934.
McManus J.F., Oppo D.W., Cullen J.L., 1999. A 0.5-Million-Year record of millennial scale climate variability in the North Atlantic. Science 283, 971-975.
Meckler A.N., Ziegler M., Millan M.I., Breitenbach S.F.M., Bernasconi S.M., 2014. Long-term performance of the Kiel carbonate device with a new correction scheme for clumped isotope measurements. Rapid Commun. Mass Spectrom. 28, 1705-1715.
Meckler, A.N., Affolter, S., Dublyansky, Y., Krüger, Y., Vogel, N., Bernasconi, S.M., Frenz, M., Kipfer, R., Leuenberger, M., Spötl, C., Carolin, S., Cobb, K.M., Moermann, J., Adkins, J.F., Fleitmann, D., 2015. Glacial-interglacial temperature change in the tropical West Pacific: A comparison of stalagmite-based paleo-thermometers. Quat. Sci. Rev., 127 (1), 90-116.
Nehme C., Verheyden S., Noble S. R., Farrant A.R., Sahy D., Hellstrom J., Delannoy J.J., Claeys P., 2015. Reconstruction of MIS 5 climate in the central Levant using a stalagmite from Kanaan Cave, Lebanon. Clim. Past, 11(12), 1785-1799.
Nehme C., Verheyden S., Breitenbach S.F., Gillikin D.P., Verheyden A., Cheng H., Noble S., Farrant A., Sahy, D., Salem Gh, Ph. Clayes, 2018. Climate dynamics during the penultimate glacial period recorded in a speleothem from Kanaan Cave, Lebanon (central Levant). Quat. Res., 90(1), 10-25.
Nehme C., Verheyden S., Nader F. H., Adjizian-Gerard J., Genty D., De Bont K., Clayes, P., 2019. Cave dripwater isotopic signals related to the altitudinal gradient of Mount-Lebanon: implication for speleothem studies. Int. J. Speleol., 48(1), 8.
NEEM, 2013. Eemian interglacial reconstructed from a Greenland folded ice core, Nature 493, 489–494.
North Greenland Ice Core Project members, 2004. High-resolution climate record of Northern Hemisphere climate extending into the Last Interglacial period. Nature 431, 147–151.
Oppo D.W., Keigwin L.D., McManus J.F., 2001. Persistent suborbital climate variability in MIS5 and Termination II. Paleoceanography 16, 280–292.
Otto-Bliesner B.L., Rosenbloom N., Stone E.J., McKay N.P., Lunt D.J., Brady E.C., Overpeck J.T., 2013. How warm was the last interglacial? New model–data comparisons. Philosophical Transactions of the Royal Society A: Mathematical, Physical and Engineering Sciences, 371(2001), 20130097.
Regattieri E., Zanchetta G., Drysdale R.N., Isola I., Hellstrom J.C., Roncioni A., 2014. A continuous stable isotope record from the penultimate glacial maximum to the Last Interglacial (159–121 ka) from Tana Che Urla Cave (Apuan Alps, central Italy). Quat. Res., 82, 450–461.
Richards D.A. and Dorale J.A., 2003. Uranium-series chronology and environmental applications of speleothems. Rev. in Mineral. and Geochem. 52, 407–460.
Rodríguez-Sanz L., Bernasconi S.M., Marino G., Heslop D., Mueller I.A., Fernandez A., Grant K.M., Rohling E.J., 2017. Penultimate deglacial warming across the Mediterranean Sea revealed by clumped isotopes in foraminifera. Sci. Rep. 7, 16572.
Rohling E.J., Cane T.R., Cooke S., Sprovieri M., Bouloubassi I., Emeis K.C., Schiebel R., Kroon D., Jorissen F.J., Lorre A., Kemp A.E.S., 2002. African monsoon variability during the previous interglacial maximum, Earth Planet Sci. Lett., 202, 61– 75.
Rohling E.J., Marino G., Grant K.M., 2015. Mediterranean climate and oceanography, and the periodic development of anoxic events (sapropels), Earth Sci. Rev., 143, 62–97.
Roucoux K.H., Tzedakis P.C., Lawson I.T., Margari V., 2011. Vegetation history of the penultimate glacial period (marine isotope stage 6) at Ioannina, north-west Greece. J. of Quat. Sci. 26, 616–626.
Rowe P.J., Wickens L.B., Sahy D., Marca A.D., Peckover E., Noble S., Özkul M., Baykara M.O., Millar I.L., Andrews J.E., 2020. Multi-proxy speleothem record of climate instability during the early last interglacial in southern Turkey. Palaeogeogr. Palaeoclim., Palaeoecol, *538*, 109422.
Rozanski K., Araguas L., Gonfiantini R., 1993. Isotopic patterns in modern global precipitation, in: Climate Change in Continental Isotopic Record, Geophysical Monograph Series, Washington DC, AGU, 78, 1–37.
Schwarcz, H.P., 1989. Uranium series dating of Quaternary deposits. Quat. Int., 1, 7–17.
Scholz, D., Kluge, T., Marx, T., Spötl, C., Schröder-Ritzraun, A., Riechelmann, D., Aeschbach-Hertig, W., Mangini, A., Richter, D.K., Niggemann, S., 2009. Temporal gradient between temperature and the oxygen isotope value of precipitation in the realy Eemian reconstructed from a sepleothem in western Germany. Geophys. Res. 11 abstract.
Scrivner A.E., Vance D., and Rohling E. J., 2004. New neodymium isotope data quantify Nile involvement in Mediterranean anoxic episodes, Geology, 32, 565–568, 2004.
Stocker T.F. and Johnsen S.J., 2003. A minimum thermodynamic model for the bipolar seesaw. Paleoceanography 18, 1087.
Thompson W.G. and Goldstein S.L., 2006. A radiometric calibration of the SPECMAP timescale. Quat. Sci. Rev., 25, 3207-3215.

Tremaine D.M., Froelich P.N., Wang Y., 2011. Speleothem calcite farmed in situ: Modern calibration of $\delta^{18}O$ and $\delta^{13}C$ paleoclimate proxies in a continuously-monitored natural cave system. Geochim. Cosmochim. Acta 75, 4929–4950.

Tzedakis P.C., Frogley M.R., Heaton T.H.E.,2003. Last interglacial conditions in southern Europe: evidence from Ioannina, northwest Greece. Glob. Planet. Change 36, 157–170.

Tzedakis P.C., Roucoux K.H., de Abreu L., Shackleton N.J., 2004. The duration of forest stages in southern Europe and interglacial climate variability. Science 306, 2231–2235.

Tzedakis P.C., Pälike H., Roucoux K.H., de Abreu L., 2009. Atmospheric methane, southern European vegetation and low-mid latitude links on orbital and millennial timescales. Earth Planet Sci. Lett., 277, 307–317.

Uemura R., Y. Matsui K. Yoshimura H. Motoyama, Yoshida N., 2008. Evidence of deuterium excess in water vapor as an indicator of ocean surface conditions, J. Geophys. Res., 113, D19114,

Uemura R., Kina Y., Shen C.-C., Omine K., 2020. Experimental evaluation of oxygen isotopic exchange between inclusion water and host calcite in speleothems. Clim. Past, 16, 17-27.

Van Geldern R. and Barth Johannes A.C., 2012. Optimization of instrument setup and post-run corrections for oxygen and hydrogen stable isotope measurements of water by isotope ratio infrared spectroscopy. Limnology Oceanography Methods 10, 1024–1036.

Verheyden S., Nader F.H., Cheng H.J., Edwards L.R., Swennen R., 2008a. Paleoclimate reconstruction in the Levant region from the geochemistry of a Holocene stalagmite from the Jeita cave, Lebanon. Quat. Res. 70(3), 368-381.

Verheyden S., Genty D., Cattani O., van Breukelen M.R., 2008b Water release patterns of heated speleothem calcite and hydrogen isotope composition of fluid inclusions. Chem. Geol., 247(1-2), 266-281.

Verheyden S., Genty D., Deflandre G., Quinif Y., Keppens E., 2008c. Monitoring climatological, hydrological and geochemical parameters in the Pere Noel cave (Belgium): implication for the interpretation of speleothem isotopic and geochemical time-series. Int. J. of Speleol., 37(3), 221-234.

Vonhof H.B., van Breukelen M.R., Postma O., Rowe P. J., Atkinson T.C., Kroon D., 2006. A continuous-flow crushing device for on-line δ^2H analysis of fluid inclusion water in speleothems. Rapid Commun. Mass Spectrom., 20(17), 2553-2558.

Waelbroeck C., Labeyrie L., Michel E., Duplessy J.C., McManus J.F., Lambeck K., Labracherie M., 2002. Sea-level and deep-water temperature changes derived from benthic foraminifera isotopic records. Quat. Sci. Rev., 21(1-3), 295-305.

Wainer K., Genty D., Daeron M., Bar-Matthews M., Vonhof H., Dublyansky Y., Pons- Branchu E., 2011. Speleothem record of the last 180ka in Villars cave (France): investigation of a large $\delta^{18}O$ shift between MIS6 and MIS5. Quat. Sci. Rev., 30, 130–146.

Wang Y.J., Cheng H., Edwards R.L., Kong X.G., Shao X., Chen S., Wu J.Y., Jiang X.Y., Wang X.F., An Z.S., 2008. Millennial and orbital-scale changes in the East Asian monsoon over the past 224,000 years. Nature 451, 1090–1093.

Wang P., Jun T., Lourens L.J., 2010. Obscuring of long eccentricity cyclicity in Pleistocene oceanic carbon isotope records. Earth Planet Sci. Lett., 290, 3-4: 319-330.

Weise A. and Kluge T., 2020. Isotope exchange rates in dissolved inorganic carbon between 40°C & 90°C. Geochim. Cosmochim. Acta, 268, 56-72.

Weißbach, T., 2020. Spectroscopic isotope ratio analysis on speleothem fluid inclusions - analytics and paleoclimatic case studies. PhD thesis, Heidelberg University, 225 pages. https://doi.org/10.11588/heidok.00028559

Ziegler M., Tuenter E., Lourens L.J., 2010. The precession phase of the boreal summer monsoon as viewed from the eastern Mediterranean (ODP Site 968). Quat. Sci. Rev., 29, 1481–1490.